Res-CN: hydrometeorological time series and landscape attributes across 3254 Chinese reservoirs

Youjiang Shen[1], Karina Nielsen[2], Menaka Revel[3], Dedi Liu[4], Dai Yamazaki[1,3]

[1]Department of Civil Engineering, Graduate School of Engineering, The University of Tokyo, Tokyo, 113-0033, Japan
[2]DTU Space, National Space Institute, Technical University of Denmark, 2800, Kongens Lyngby, Denmark
[3]Global Hydrological Prediction Center, Institute of Industrial Science, The University of Tokyo, Tokyo, 153-8505, Japan
[4]State Key Laboratory of Water Resources & Hydropower Engineering Science, Wuhan University, Wuhan, 430072, China

Correspondence to: Youjiang Shen (yjshen2022@rainbow.iis.u-tokyo.ac.jp)

Abstract. Dams and reservoirs are human-made infrastructures that have attracted increasing attentions because of their societal and environmental significance. Towards better management and conservation of reservoirs, a dataset of reservoir-catchment characteristics is needed, considering that the amount water and material flowing into and out of reservoirs depends on their locations on the river network and the properties of upstream catchment. To date, no dataset exists for reservoir-catchment characteristics. The aim of this study is to develop the first database featuring reservoir-catchment characteristics for 3254 reservoirs with storage capacity totaling 682,595 km³ (73.2% reservoir water storage capacity in China), to support the management and conservation of reservoirs in the context of catchment level. To ensure a more representative and accurate mapping of local variables of large reservoirs, reservoir catchments are delineated into full catchments (their full upstream contributing areas) and intermediate catchments (subtracting the area contributed by upstream reservoirs from full upstream of the current reservoir). Using both full catchments and intermediate catchments, characteristics of reservoir catchments were extracted, with a total of 512 attributes in six categories (i.e., reservoir catchment, topography, climate, soil and geology, land cover and use, and anthropogenic activity). Besides these static attributes, time series of 15 meteorological variables of catchments were extracted to support hydrological simulations for a better understanding of drivers of reservoir environment change. Moreover, we provide a comprehensive and extensive reservoir data set on water level (data available for 20% of 3,254 reservoirs), water area (99%), storage anomaly (92%), and evaporation (98%) from multisource satellites such as radar and laser altimeters and images from Landsat and Sentinel satellites. These products significantly enhance spatial and temporal coverage in comparison to existing similar products (e.g., 67% increase in spatial resolution of water level and 225% increase in storage anomaly) and contribute to our understanding of reservoir properties and functions within the Earth system by incorporated national or global hydrological modeling. In situ data of 138 reservoirs are employed in this study as a valuable reference for evaluation, thus enhancing our confidence in the data quality and enhancing our

understanding of accuracy of current satellite datasets. Along with its extensive attributes, the Reservoir dataset in China (Res-CN) can support a broad range of applications such as water resources, hydrologic/hydrodynamic modeling,
35   and energy planning. Res-CN is on Zenodo through https://doi.org/10.5281/zenodo.7390715 (Shen et al., 2022a).

1 Introduction

The role of reservoirs in the hydrological and biogeochemical cycles is closely tied to their characteristics of water area, water level, evaporation, and storage variation. In addition, the amount and rate of water flowing into and out of reservoirs depends on their location in the river network, reservoir upstream catchment attributes (e.g., catchment
40   size, topography, geology, soil, and land cover) as well as meteorological variables (e.g., precipitation, and temperature). An explicit spatial knowledge of all these characteristics is crucial for determining surface water availability and modulating water flux interactions among various earth system components, including terrestrial water storage dynamics (Busker et al., 2019; Chaudhari et al., 2018); terrestrial carbon cycle (Marx et al., 2017); surface energy budget (Buccola et al., 2016); climate-related effects (Boulange et al., 2021); and alterations in the hydrological and
45   ecological processes such as sediment reduction (Li et al., 2020) and fish biodiversity decline (Ngor et al., 2018). Therefore, to fully uncover the functioning of reservoirs for better scientific studies and water resources managements, it is essential to develop a comprehensive publicly available reservoir data set, especially driven by climate warming and human population growth.

Remote sensing techniques enable the possibility of monitoring reservoirs from space and describing reservoir
50   characteristics around the world in the absence of accessible in situ records. Different research projects and studies have produced satellite datasets for reservoirs at regional and global scales. Hydroweb (Crétaux et al., 2011), G-REALM (Global reservoirs and lakes monitor, Birkett et al., 2011), DAHITI (Database for hydrological time series of inland waters, Schwatke et al., 2015), AltEx (Markert et al., 2019), HydroSat (Tourian et al., 2022), Water level On VITO, and several studies (e.g., Gao et al., 2012; Tortini et al., 2020; Shen et al., 2022b) offer time series of altimetry-derived water
55   level for inland waters by incorporating multiple laser or radar altimeters such as Jason-1/2/3, CryoSat-2, Sentinel-3A/B, and ICESat-1/2. Imagery-based water area estimates can be extracted from GSW (Global surface water, Pekel et al., 2016), DAHITI, Hydroweb, HydroSat, Bluedot Observatory, GRSAD (Global reservoir surface area dataset, Zhao & Gao, 2018), RealSAT (Khandelwal et al., 2022), and relevant studies (e.g., Busker et al., 2019; Liu et al., 2021; Donchyts et al., 2022). Storage anomalies are available in DAHITI, HydroSat, and several studies (e.g., Gao et al., 2012; Hou et al.,
60   2022) using water level and area from satellite altimeters and images, and/or from imagery-based water area and the area-storage model constructed by digital elevation model (DEM, Vu et al., 2022). Reservoir evaporation estimates can be obtained from the datasets developed by Tian et al. (2022) and Zhao et al. (2019; 2022), which used imagery-based water areas and meteorological forcings to calculate the evaporation estimates.

Despite great progress in previous studies and satellites with extensive data availability, information of reservoir
65   characteristics is still insufficient and scarce across different regions. At both regional and global scales, these studies
mentioned above failed to provide a comprehensive reservoir data set. The majority of them are devoted to developing
a particular type of reservoir data set (e.g., water level, water area, storage anomaly, or evaporation) for selected
globally distributed reservoirs (Gao et al., 2012; Zhao et al., 2022). For example, Zhao et al. (2019) constructed the long-
term monthly evaporation time series for 721 reservoirs in the U.S. by using four meteorological forcings and Landsat-
70   based images. Other remotely sensed datasets such as storage anomalies from (e.g., Busker et al., 2019; Hou et al., 2022)
and water areas from (Klein et al., 2021) are not publicly accessible. Remotely sensed reservoir datasets, estimated by
different researchers, are usually not consistent on the aspects of target water bodies and data sources, which make it
difficult to provide consistent baseline of reservoir characteristics for a specific region or country. For example,
Khandelwal et al. (2022) generated monthly water areas over the new lake polygons while other studies produced
75   water area time series over the reservoir/lake shapefiles from some existing databases such as GRanD (Lehner at al.,
2011) and HydroLAKES (Messager at al., 2016). In addition, there is no systematic assessment of whether reservoir
water levels or water areas from previous studies and databases agree with one another, as shown in this study by
many reservoirs whose in situ measurements are available. Here, we list remotely sensed databases containing Chinese
reservoirs in Supplementary Table S1. Only a small number of reservoirs are available from these databases. In three
80   popular altimetry-based datasets reservoirs (Hydroweb, G-REALM, and DAHITI), there are approximately 30 Chinese.
Although Shen et al. (2022b) used GRanD reservoir shapefiles and multisource altimeters to generate a data set of
water level, area, and storage anomaly for 338 Chinese reservoirs during 2010-2021, there is still room for additional
complements to the existing databases in its spatial and temporal coverage.

Apart from time series of above reservoir states, reservoir upstream catchment attributes (e.g., catchment shapefile,
85   climate, geology & soil, topography, land cover, and anthropogenic activity) are also important as reservoirs collect
materials from upstream catchments. The lake datasets and station-based datasets of catchment characteristics (e.g.,
Addor et al., 2017; Alvarez-Garreton et al., 2018; Klingler et al., 2021; Lehner et al., 2022; Liu et al., 2022) proved that
catchment-level attribute datasets are very useful. To date, no dataset exists for reservoir-catchment characteristics.
Moreover, allocating reservoirs on river network is also valuable for river models incorporating reservoirs as reservoir
90   datasets and river network datasets are usually developed independently, and they are not well corresponding and
could cause some issues when integrating reservoirs in river model.

In light of above, we build upon these existing studies and datasets to produce a new publicly available comprehensive
and extensive reservoir dataset, Res-CN (Reservoir-ChiNa). It is based on the latest reservoir shapefiles from GeoDAR
v1.1. Additionally, we allocate reservoirs on the MERIT Hydro (Yamazaki et al., 2019) to delineate reservoir catchments
95   into two categories: full catchments and intermediate catchments. 512 catchment-level attributes for 3254 reservoirs
are generated at full catchments and intermediate catchments from a wide range of satellite-, reanalysis-, and in-situ

based data. Besides, time series of reservoir states (i.e., water level, water area, storage variation, and evaporation) are extracted from multiple altimeters, Landsat and Sentinel images and other satellites, acting as a key supplement to existing products owing to its significantly enhanced spatial and temporal coverages. In situ data of 138 reservoirs are
100   employed in this study as a valuable reference for evaluation, thus enhancing the confidence in the data quality and enhancing the understanding of accuracy of current satellite datasets. Our codes, in Python/R/GEE, are freely available and open source. The code can be applied to calculate reservoir states for individual applications or other areas. Results of this study facilitated managements of reservoirs and relevant studies such as hydrological modeling, environmental studies, and climate research in the spatially explicit context of reservoir catchment-level.

105   **2 Data sources and methods**

China has more than 98,000 reservoirs and dams across different topographic regions and landscapes. However, most of them are unmapped (polygons and georeferenced coordinates not available) and only described with standard attributes. Thus, in this study, we focused on reservoirs for which are mapped and available from the newest global GeoDAR database (Wang et al., 2022). GeoDAR v1.1 provides global reservoir shapefiles and their attributes such as
110   storage capacity, reservoir purpose and installed capacity. Reservoirs are mostly clustered in Yangtze and Pearl River basins (Fig. 1) and vary greatly in size, capacity, and purpose.

As we aim to create a comprehensive reservoir data set in China, our workflow required multiple steps and geospatial techniques. Here, we detail the data and methodologies that is applied to create water level, area, storage variation, evaporation, upstream catchment boundaries and catchment-level characteristics. The flowcharts and source datasets
115   are provided in the Figures A1-2, Figures S4-6, and Table S2-8.
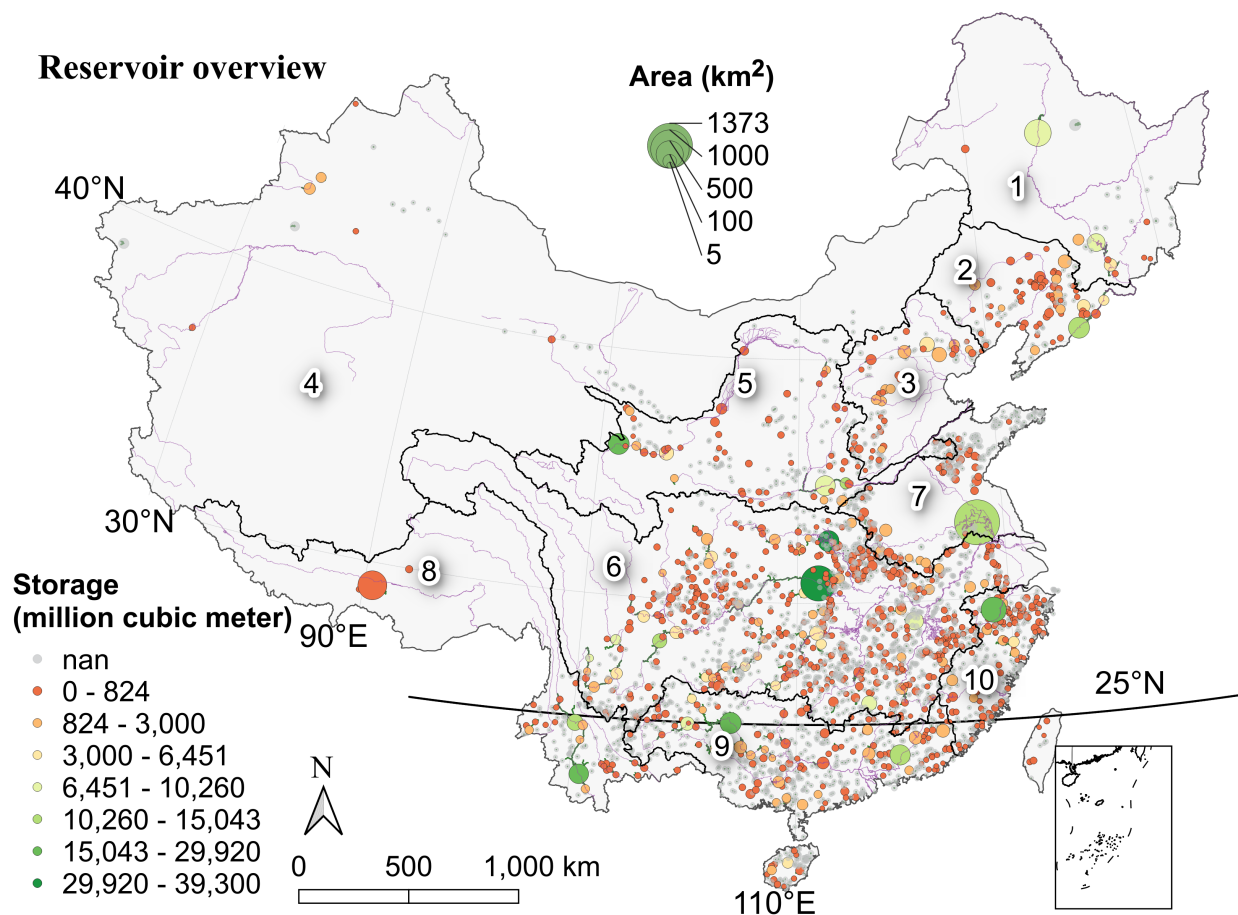
Figure 1. Overview of the reservoirs contained in Res-CN, and the dams with storage capacity (circle color, nan means not available) and water area of reservoirs (circle size). The black lines indicate the boundaries of the ten river regions within Res-CN. Numbers (1-10) indicate: 1—Songhua River; 2—Liao River; 3—Hai River; 4—Northwest River; 5—Yellow River; 6—Yangtze River; 7—Huai River; 8—Southwest River; 9—Pearl River; and 10—Southeast River regions.

2.1 Data and methodology for generating reservoir water level

Water level time series for the Res-CN reservoir are derived from various satellite altimeters: Sentinel-3A, Sentinel-3B, Jason-3, ICESat-2, CroySat-2, and SARAL/AltiKa. Each altimeter has different repeat cycles, geographical coverages, retracking algorithms, and measurement accuracies (Table S2). Apart from the official algorithms in their source products, we implemented PPCOG (primary peak center of gravity) and NPPTr[0.5/0.8] (narrow primary peak with a 0.5 or 0.8 threshold value) algorithms into Sentinel-3, CroySat-2, SARAL/AltiKa to derive range measurements (Shen et al., 2022b). Range measurements are corrected using the atmospheric and geophysical corrections from their source products (Table S2), and then used to determine water level of each sample. We reference the height to the EGM2008 geoid (Pavlis et al., 2012).

130   For the construction of reservoir water levels, we carried out the following steps to process single satellite altimetric heights from each retracking algorithm (Fig. S4):

- Extraction of the altimetric data within the GeoDAR reservoir shapefile.
- Selection of altimetric data whose water occurrence larger than 10% using the Global Surface Water Explorer.
- Outlier removal for each pass using the MAD method (median of absolute deviation).
135   - We remove outliers from altimeter data with heights more than 20 meters from the DEM (for reservoirs with large variations, we set a threshold of 40 meters).
- Construction of time series using the R package "tsHydro" (Nielsen et al., 2015).

Through these steps, each satellite altimeter's SR (standard rate) water level time series with different retracking algorithms were produced. A single satellite altimeter's repeat period and spatial sampling results in a low resolution
140   for SR products. For example, with Sentinel-3A ground tracks spaced 104 km apart at the equator, it may be possible to obtain altimetric data on 684 GeoDAR reservoirs in China. For increased resolution and to overcome the limitations of single satellite altimeter spatial and temporal sampling, we generated HR (high rate) water level time series products by integrating single-satellite SR products. Note that we used altimetric observations from multi-mission using the retracking algorithm with the smallest RMSE (root-mean-square error) value calculated with in situ water level. To
145   eliminate systematic differences between satellites, we used two methods: the first method is by directly eliminating the mean water level differences between satellites and is applicable to satellites with sufficient overlap periods; the second method is to estimate satellite bias using reservoir water areas. The bias was estimated by minimizing the two-dimensional cost function of area-water level coordinates using the Gauss-Helmert method (Fig. S4). To evaluate the altimetric data quality, we calculated the standard deviation (SD) of altimetric observations and RMSE values against
150   in situ water level and three other similar existing products from Hydroweb, DAHITI, and G-REALM wherever available. Data point precision is determined by SD, whereas accuracy is determined by RMSE. RMSE is calculated by comparing water level anomalies between gages and satellites. In situ water level of 99 reservoirs from 2015 to 2021 are used to validate our dataset.

2.2 Data and methodology for generating reservoir water area

155   Reservoir water areas can be extracted from an available global inland water dataset like the SWBD (SRTM Water Body Data, NASA JPL, 2013), the GIEMS (Global Inundation Extent from Multiple Satellites, Papa et al., 2010b), GSW, DAHITI, Hydroweb, Hydrosat, Bluedot Observatory and studies from Tortini et al. (2020) and Shen et al. (2022b). The derived reservoir water area estimations are limited by the spatial coverage and accuracy restrictions of the initial dataset. As such, three available global water area products are developed by using algorithms that reclassify contaminated pixels
160   as water, i.e., the GRSAD (Zhao & Gao, 2018), the RealSAT (Khandelwal et al., 2022), and areas of medium-small reservoirs by Donchyts et al. (2022). These products cover only a portion of the reservoirs we studied (e.g., 908

overlapping reservoirs between GRSAD and our product) and use different algorithms and source datasets (e.g., RealSAT and GRSAD use only Landsat). As a part of this study, we employed the algorithm developed by Donchyts et al. (2022) to generate reservoir water areas by using Landsat and Sentinel-2 images. There is good evidence that this

165 algorithm maps reservoir water areas well in 768 reservoirs of various sizes and climate zones. For a given reservoir, the procedures are as follows:

- A selection of cloudy satellite images intersecting the reservoir shapefile is made.
- Based on the global cloud frequency dataset (Wilson, 2016), filter out satellite images that are completely covered by clouds and correct the remaining images as follows.

170 - NDWI (normalized difference water index) calculation.
- A Canny edge detection algorithm is used for detecting water/land edges and defining sampling areas around them (Donchyts et al., 2016).
- Utilizing the Otsu algorithm (Markert et al., 2020) to determine the optimal threshold value, then obtaining the water mask based on samples of NDWI values collected within the sampling area.

175 - Sampling the water occurrence along the edges to eliminate falsely detected water (water pixels that were not water).
- Water occurrence is clipped at a certain occurrence value and combined with water mask to obtain the final water mask.
- Using a quantization-based temporal outlier filter to remove any errors from reservoir waters.

180 Using these procedures, we generated monthly reservoir water areas during 1984-2021. We evaluated the data quality by comparing it to in-situ water levels, altimetry (HR and SR products) whenever available, and previously available products from GRSAD and RealSAT. The indicators of data quality were rBIAS (relative bias), CC, and rRMSE (relative RMSE).

2.3 Data and methodology for generating reservoir storage variation

185 Res-CN estimates of reservoir storage variation are based on (1) satellite-based water levels and water areas, and (2) water areas and DEMs (digital elevation models) (Fig. S5). The basis of these two approaches is a reconstruction of the hypsometry curve (water area-level model) using overlapping records of water level and area or DEM. Assuming five models (linear, polynomial, exponential, power, and logarithmic) can be used to describe hypsometry curves, we selected the model with the highest R^2 value as the reservoir's hypsometry curve. We followed the following steps for

190 reservoirs with both water levels and areas records:

- Using the average of all altimetric measurements in a month to calculate the monthly reservoir water level.
- A scatterplot of monthly water level and area is constructed, and errors are eliminated from the scatterplot.
- A parametric approach is used to generate the hypsometry curve (i.e., the water area-level model).

- Estimating the gap measurements of water levels and areas by applying the reconstructed hypsometry curve.
195
- Calculating storage variation ΔV from two successive pairs of water level-area measurements (H, A), Eq. (1)

$$\Delta V_t = \frac{1}{2}(H_t - H_{t-1}) \times (A_t + A_{t-1}), \tag{1}$$

For reservoirs with water areas only, we used the DEM-based approach. The main procedures are described below:

- Generating the water area-level-storage model through DEM-based approach (Vu et al., 2022).
- Calculating storage variation by combining satellite-based water areas and area-level-storage model.

200 As a result of these steps, we determined the hypsometry curve and time series of storage variations for each reservoir. To evaluate the storage variation data, we calculate the error statistics of RMSE, NRMSE (normalized root-mean-square error), and CC (pearson correlation coefficient) values for reservoirs with in situ observations. In situ water storage of 138 reservoirs from 2015 to 2021 are used to validate our dataset.

2.4 Data and methodology for generating reservoir evaporation

205 Reservoir evaporation estimates can be extracted from two available global reservoir evaporation products produced by the Zhao et al. (2022) and Tian et al. (2022). These studies covered a portion of the reservoirs we studied and used the same robust algorithm by Zhao et al. (2019) to calculate monthly reservoir evaporation volume (V_E, [m³/month]) using water area (A, [km²]), days of a month (*days*, [-]), and evaporation rate ($E_{reservoir}$, [mm/day]) (Eq. 2).

$$V_E = E_{reservoir} \times A \times days/1000 \tag{2}$$

210 In this study, we applied the algorithm as well considering its satisfactory simulation performance for the evaporation rate and energy balance terms (Eqs. 3-4). It quantifies heat storage changes (δU, [MJ m⁻² d⁻¹]) in the Penman equation

$$E_{reservoir} = \frac{\Delta(R_n - \delta U) + \gamma\lambda(2.33 + 1.65u_2)L_f^{-0.1}(e_s - e_a)}{\lambda(\Delta + \gamma)} \tag{3}$$

$$\delta U = \rho_w c_w h \frac{T_w - T_{w0}}{\Delta t} \tag{4}$$

where $E_{reservoir}$ is the reservoir evaporation rate (mm/d); Δ is the slope of the saturation vapor pressure curve
215 (kPa/°C); R_n is the net radiation (MJ m⁻² d⁻¹); γ is the psychrometric constant (kPa/°C); λ is the latent heat of vaporization (MJ/kg); u_2 is the wind speed at 2 m height (m/s); and L_f is the monthly reservoir fetch length (m); e_s and e_a are the saturated vapor pressure at air temperature and the air vapor pressure (kPa), respectively; ρ_w is the density of water (kg m⁻³); c_w is the specific heat of water (MJ kg⁻¹ °C⁻¹); h is the average water depth (m); T_w and T_{w0} are the water column temperature at the current time step, and at the previous time step (°C), respectively; and Δt is the time
220 step (set as 1 month in this study).

It is worth noting that this algorithm does not need parameter calibration and only requires the L_f, h, and four meteorological variables (air temperature [°C], wind speed [m/s], vapor pressure deficit [kPa], and surface downward

shortwave radiation [MJ m^{-2} d^{-1}]), for the evaporation rate calculation. In previous studies (Zhao et al., 2022; Tian et al., 2022), the TerraClimate dataset (Abatzoglou et al., 2018) has been shown to be the most appropriate meteorological
225 dataset for reliable estimates of reservoir evaporation rates compared to other global datasets. Thus, we adopted the TerraClimate to generate meteorological data time series by averaging gridded forcing data within reservoir shapefiles. Monthly reservoir fetch values L_f were calculated using (1) reservoir shapefile, (2) wind direction data from the NCEP (National Centers for Environmental Prediction), and (3) water area time series. The average reservoir water depths h are taken from the GRanD and HydroLAKES datasets. For reservoirs not recorded in these two datasets, we determined
230 their water depths from their water areas through the area-depth curves fitted to all available data. A detailed algorithm flowchart, all equations, and examples are provided in the Figure S6 and Zhao et al. (2019).

2.5 Data and methodology for generating reservoir catchment boundaries

In this study, two types of reservoir upstream catchment boundaries (hereafter, referred to as catchment) are defined: full catchments and intermediate catchments (Fig. 2). The full catchment is defined as a reservoir's full upstream
235 contributing area, whereas the intermediate catchment is determined by subtracting the area contributed by upstream reservoirs from the catchment area of the current reservoir. Obviously, full catchments are independent with each other, but for reservoirs with larger catchments, they can lead to a significant loss of information such as the local features and variability. Thus, intermediate catchments, which are part of the large river networks, can complement this information and ensures more representative and accurate mapping of local variables.
240 To identify catchment boundaries (Fig. A1), we used an automatic outlet relocation algorithm (Xie et al., 2022) to automatically delineate a large amount of catchments. This algorithm can correct the river networks by analyzing the gradients of flow accumulations along the rivers and can rapidly delineate catchments, e.g., taking 58 minutes to delineate 1,398 catchments. More importantly, it has been intensively validated in 1,398 catchments of varying size and geographic regions, showing 94.1% of catchments were correctly delineated. This algorithm requires the flow
245 directions and gauge locations as input. In this study, we used flow directions from the MERIT Hydro and dam locations from the GeoDAR dataset. MERIT Hydro is a new global hydrography map that has a fine resolution of 90 m and shows good performance in terms of river basin shape and flow accumulation area. This algorithm can generate the full catchments of each reservoir, and we employed some additional operations to remove topology errors and obtain intermediate catchments. Firstly, we cleared the holes to remove topology errors across full catchments. Secondly, we
250 checked the full catchments, and removed the unrealistic or incorrectly catchments. Thirdly, we generated intermediate catchments by removing the overlapping areas of upstream reservoirs from the full catchment of the current reservoir using QGIS 3.24. Lastly, we fixed the invalid geometry of intermediate catchments by eliminating geometry errors (Supplementary Text 1).

a) Basin delineation A | Full catchments
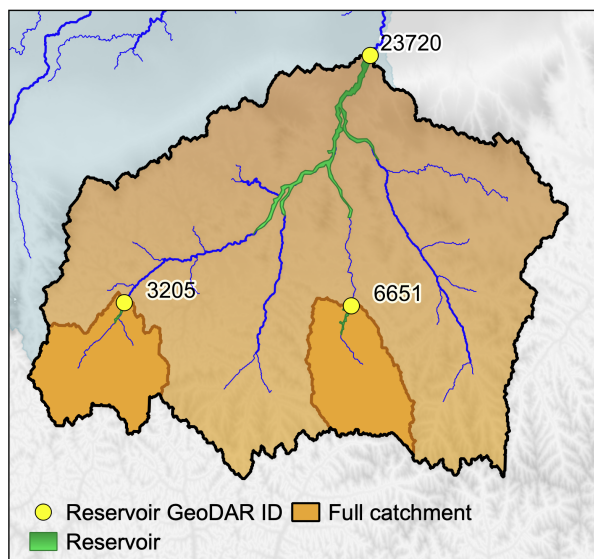
b) Basin delineation. B | Intermediate catchments
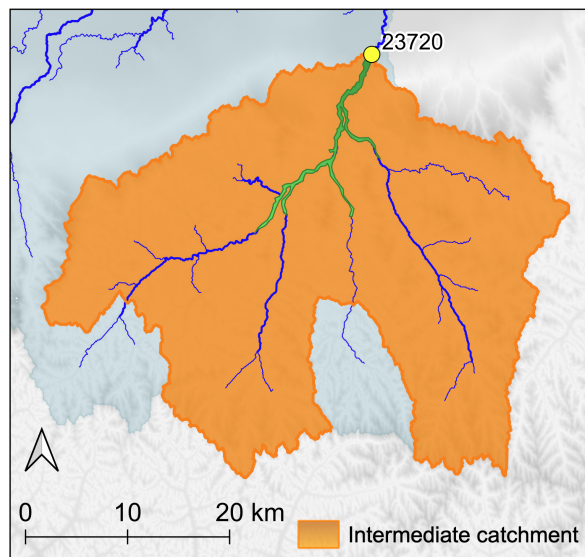
Figure 2. An example of the types of catchment delineations in Res-CN. (a) Catchment delineation A: full catchments, which are defined as the entire area contributing to a reservoir. In plot (a), full catchment of reservoir 23720 overlaps with that of reservoir 3205 and that of 6651. (b) Catchment delineation B: intermediate catchment. In plot (b), all upstream contributing areas of the upstream reservoirs (3205 and 6651) are removed from the full catchment of reservoir 23720, thus, we get the intermediate catchment of reservoir 23720 (in black boundary). Background in light blue indicates other catchments not shown in this example. Source of background: MERIT Hydro and MERIT DEM (Yamazaki et al., 2019).

2.6 Data and methodology for generating catchment-level characteristics

To facilitate the use of our Res-CN and promote common standards in large sample studies, we computed catchment attributes introduced by Addor et al. [2017] in their Catchment Attributes and MEteorology for Large-sample Studies (CAMELS) and many followed up studies such as CAMLES-CL, CMALES-BR, CAMLES-GB, CCAM, LamaH-CE, LakeALTAS and studies by Chen et al. (2022) and Liu et al. (2022) and added several other attributes. These attributes can be categorized into six types: reservoir and catchment shapefile, climate, geology & soil, topography, land cover and anthropogenic activity. The sources for different datasets were chosen to ensure use of high-quality, most reputable, global coverage, theoretical impacts on reservoirs, and high spatial resolution as far as possible. For example, the NSCD version 3 (National station-based climatic data set) is the most widely used in situ meteorological dataset in China, while the MERIT DEM is a new baseline of global hydrography map. Here, we give a brief description of data processing, while the detailed interpretations, uncertainties, and limitations of source datasets are available in Section 3 and Supplementary (Fig. A2).

Some necessary data format conversions (e.g., netCDF to raster format) and reprojections are firstly conducted for related attribute datasets. Then, we used different methods to calculate catchment-level characteristics from raster and vector data. Statistics values were calculated for raster grids within each catchment. In the case of continuous variables such as temperature and elevation, we calculated their mean, maximum, minimum, and range values. For categorical variables such as geological maps and land use features, we calculated the percentages of each variable and determined their dominant type. The implementation for processing raster data is done in the local Python and R environments (package: rasterstats) and the GEE platform. For vectorial data such as the rivers and catchments in ESRI shapefile format, the shape features of each catchment are calculated using the local Python scripts, and other catchment attributes like stream density are determined by the ratio of the intersection area between the vectorial data and the catchment extent layer to the total catchment area. After repeating these procedures for each catchment, catchment-level attributes are prepared for both full catchments and intermediate catchments.

3 Results and discussion

3.1 Description of the Res-CN database

We here provide a summarized information on the components of the Res-CN in Table 2. Detailed descriptions of each component are shown in the following sections and Supplementary materials. In this study, we constructed reservoir-catchment characteristics for 3254 reservoirs with water areas ranging from 0.004 and 1373.77 km^2, with storage capacity totaling 682,595 km^3 (i.e., 73.2% reservoir water storage capacity in China). Using both full catchments and intermediate catchments, characteristics of reservoir catchments were extracted, with a total of 512 attributes in six categories (Table 2). Besides, time series of reservoir states such as water level and area are also provided. For more details, please refer to the data repository and the following sections.

Table 2. Summary of the data provided in the Res-CN.

	Variable	Number of (reservoirs/catchments)	Description
Time series of reservoir states	Water level (SR, a total of 650 reservoirs)	54	From Jason-3, 10-days, 2016-2022, with 3 retracking algorithms
		192	From Sentinel-3A, 27-days, 2016-2022, with 5 retracking algorithms
		194	From Sentinel-3B, 27-days, 2018-2022, with 5 retracking algorithms
		215	From ICESat-2, 90-days, 2019-2022, with 1 retracking algorithm
		347	From CryoSat-2, 369-days, 2010-2022, with 3 retracking algorithms
		229	From SARAL/AltiKa, 35-days, 2016-2022, with 5 retracking algorithms
	Water level (HR)	250	High rate (HR) product by merging SR products, from 2010-2022, sub-monthly or monthly

	Water area	3214	Monthly from 1984-2021
	Storage variation	2999	Monthly storage variation from 1984-2021
	Evaporation	3185	Monthly evaporation rate and volume from 1984-2021
Catchment-level attributes	Reservoir and catchment shapefile	3254 full catchments, 435 intermediate catchments, 3254 reservoirs	Two types of reservoir upstream catchments, reservoir and catchment shapefile attributes (Tables S9-10)
	Topography	3689 (full and intermediate catchments)	19 attributes (Table S10)
	Climate data	Same as above	11 climatic attributes and daily time series of metrological data with 15 variables from 1980-2022 (Tables S11-12)
	Land cover	Same as above	21 attributes (Table S13)
	Soil & Geology	Same as above	173 attributes (Tables S14-15)
	Anthropogenic activity	Same as above	288 attributes (Table S16)

3.2 Res-CN products for catchment shapefile characteristics

295   Res-CN provides 3254 full catchments and 435 intermediate catchments (Fig. 3). The median catchment size of full catchments is 294 km², with a range of 0.94 to 981,473 km². The plausibility of full catchment delineation was assessed by comparing the area of the delineated catchments with the areas of two declared references: GRanD (Lehner et al., 2011) and LakeATLAS (Lehner et al., 2022). LakeATLAS delineated upstream drainage area of more than 1.4 million lakes and reservoirs globally based on the lake pour points and the 15 arc-seconds drainage direction grids of

300   HydroSHEDS. A similar approach was applied in the GRanD to estimate the areas of upstream catchments over 7,320 reservoirs globally. To compare Res-CN with GRanD and LakeATLAS, we spatially joined reservoir shapefiles from both datasets, matching reservoirs that overlapped for greater than 90% of their extent. Based on this subset of reservoirs, we found that catchment areas delineated in this study corresponded relatively well to catchment areas in both GRanD (CC = 0.99, n = 910) and LakeATLAS (CC = 0.90, n = 2147), which proves the reliability of our delineated catchments.

305   Large discrepancies occur in 55 catchments, whose absolute relative error is greater than 100% (Fig. 3d, f). Small reservoirs located near confluences between rivers of different sizes are more likely to be affected by this issue, as a minor spatial mismatch can assign a reservoir to the small catchment of the tributary stream rather than the large catchment of the mainstream, and vice versa. The differences in catchment delineation between these datasets result from differences in both DEM and methods for flow direction correction and depression filling and pour points

310   correction. In this study, the widely verified MERIT Hydro flow directions are used, and we suggest that cautions should be taken when using catchments with large error discrepancies with LakeATLAS, which is based on the drainage direction grids of HydroSHED. Intermediate catchments provide information regarding the variability of local features

and upstream–downstream relationship. The median catchment size of intermediate catchment is 936 km², with a range of 1 to 279,424 km².
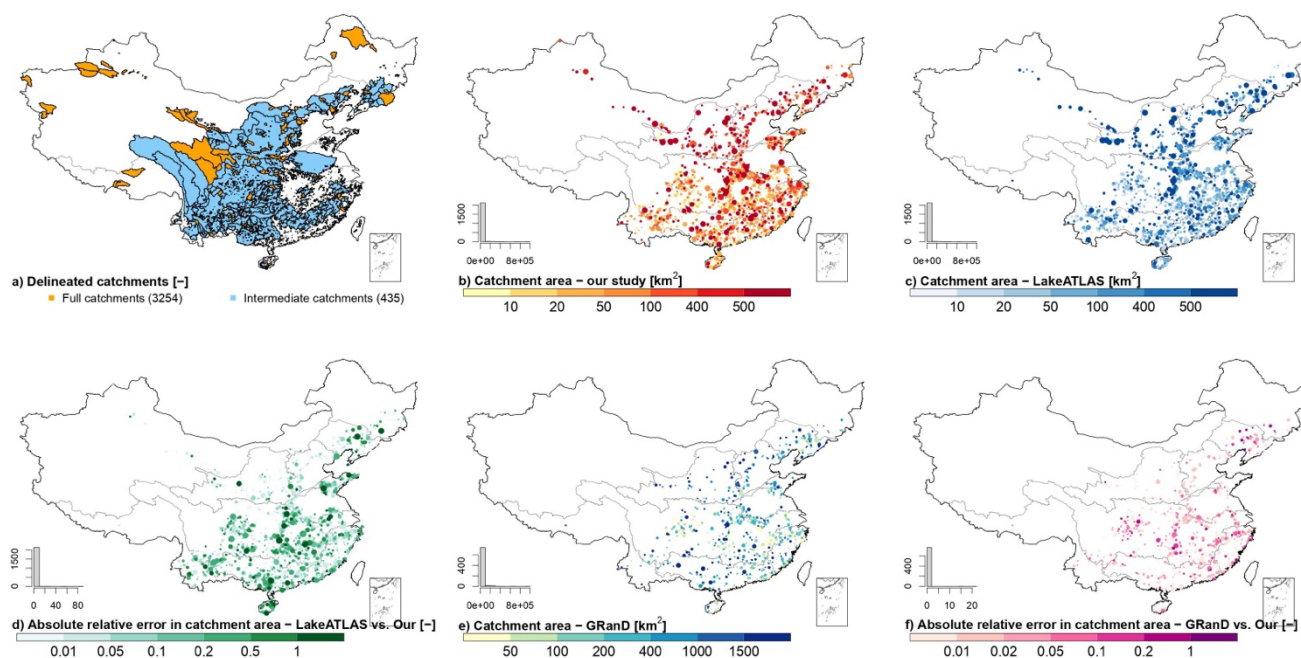
Figure 3. Distribution of the delineated catchments (intermediate catchments and full catchments). Each category's histogram indicates the number of basins (out of 3254). Circle sizes are proportional to catchment areas. In the figure caption, dimensionless is indicated by [-].

3.3 Res-CN products for time series of reservoir states

3.3.1 Reservoir water level

There are two modes of reservoir water level time series available from Res-CN, SR and HR. Fig. 4 demonstrates their spatial coverages, data source and availability, and evaluation reports against in situ observations. Among them, over 200 reservoirs are visited by CroySat-2, SARAL/AltiKa and ICESat-2, and only 192 and 54 reservoirs are covered by Sentinel 3A and Jason 3, respectively (Table 2). Data quality was generally good for smaller RMSE values (< 0.3 m), moderate for those between 0.3 and 1.0 m, and relatively poor for those greater than 1.0 m. For each altimeter and HR product, percentage of validated reservoirs with good, moderate and poor data quality is 44%,33%, 23% (Sentinel-3A: validated in 34 reservoirs), 55%, 18%, 27% (Sentinel-3B: 22), 38%, 37%, 25% (SARAL/AltiKa: 8), 71%, 10%, 19% (ICESat-2: 31), 50%, 36%, 14% (Jason-3: 14), 22%, 56%, 22% (Cryosat-2: 27), and 25%, 73%, 2% (HR products: 84). We found that in most cases there is no notable difference in terms of RMSE values between different retracking algorithms (Fig. S7). It should be noted that multisource altimetric measurements are merged for a specific reservoir by using the SR time series with the lowest RMSE from the retracking algorithm. Fig. 5 shows examples of HR products

over a sample of six reservoirs with different areas. Single-altimetric time series capture reservoir water level dynamics well, leading to improved temporal resolution of HR product. Water level time series for each reservoir are available in Rec-CN as EXCELs, PDFs and detailed evaluation reports. A cross validation of the time series against other existing

335 databases as well as a comparison of their spatial coverage in China (Table S1 and Fig. S8) further demonstrated the advantages of our products. Water levels provided by Res-CN generally agree with those provided by exsiting similar products (Hydroweb, G-REALM, and DAHITI) with CC values exceeding 0.9, although there are some discrepancies. As an example, Res-CN time series are much denser and less noisy than Hydroweb's in most reservoirs. At the Sanhezha reservoir, G-REALM failed to capture the clear fluctuation pattern, while large discrepancies were apparent at the

340 Fengman reservoir in 2020 between Res-CN and Hydroweb (Fig. S8).

We should consider some limitations for further improvements despite our products' good performance and expanded spatial coverage. In our study, more than 80% of reservoirs with inadequate altimetric measurements are removed due to the inherent limitations of satellite altimeters. There are still challenges to delivering useful measurements for certain reservoirs along the Yangtze and Yellow rivers, and data quality is poor in terms of RMSE values regardless of

345 reservoir size. It may be possible to apply advanced algorithms such as machine-learning in future studies to achieve better performance regardless of whether reservoirs represent different behaviors.
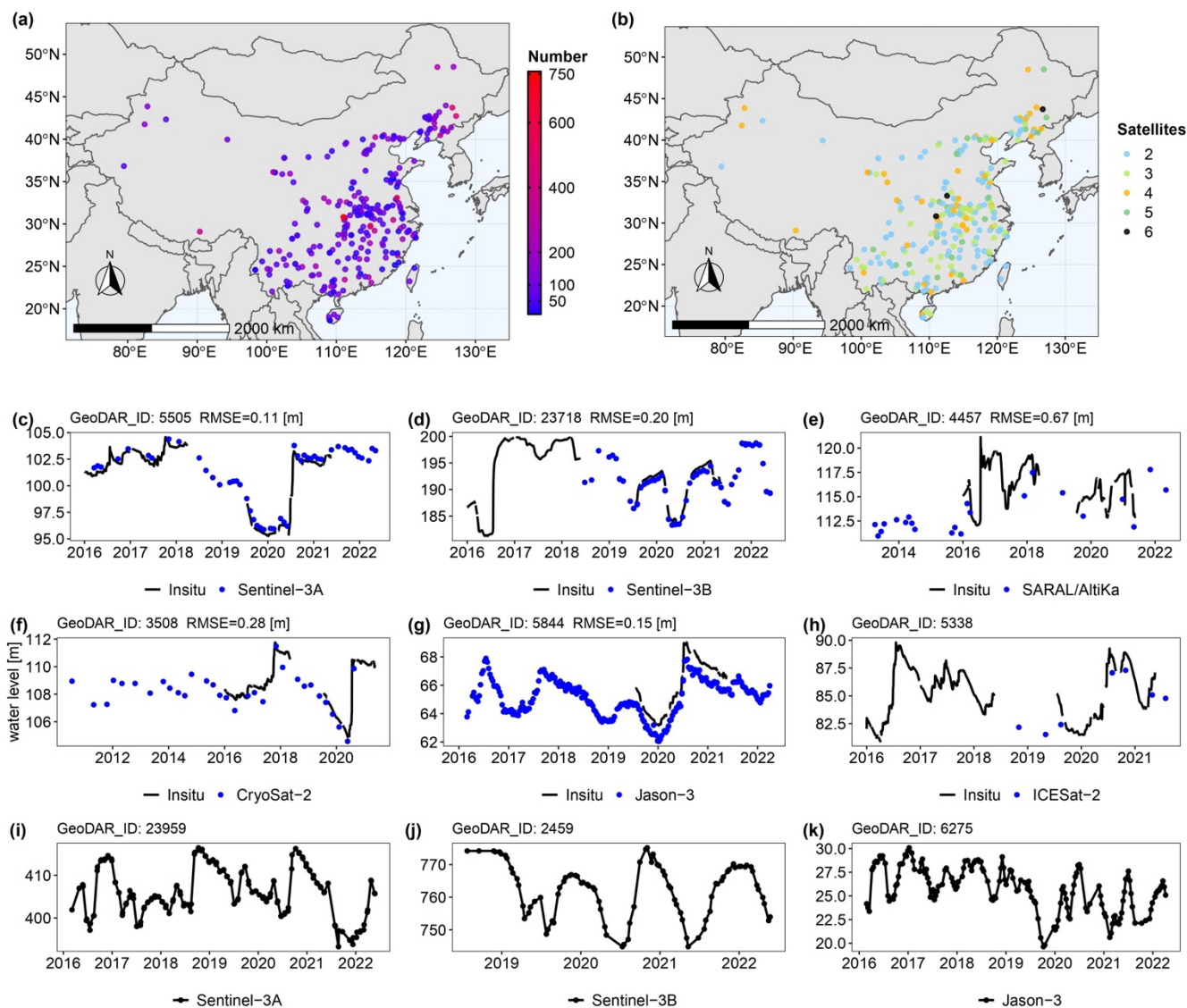
Figure 4. Data data availability of the altimetric reservoir water level time series (a) and number of satellites for High-rate products (b) as well as some examples to illustrate time series of Standard-rate products over nine selected reservoirs (c-k).
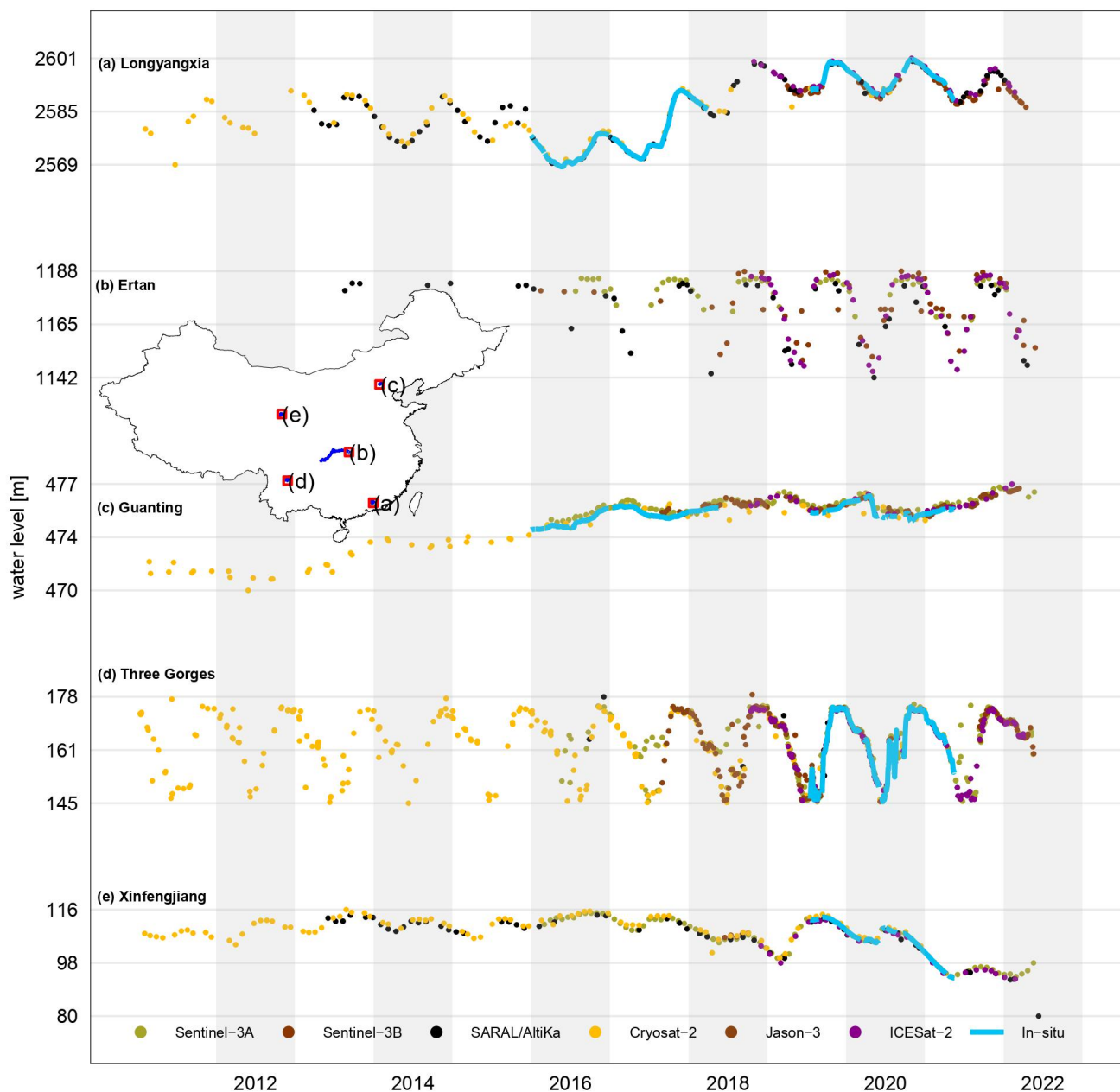
350

Figure 5. High-rate water level time series over reservoirs Xinfengjiang (264 km²) from Sentinel-3A, SARAL/AltiKa, Sentinel-3B, CryoSat-2 and ICESat-2; Three Gorges (852 km²) from Sentinel-3A, SARAL/AltiKa, Sentinel-3B, CryoSat-2, ICESat-2, and Jason-3; Guanting (90 km²) from Jason-3, CryoSat-2, ICESat-2, Sentinel-3A, and Sentinel-3B; Ertan (65 km²) from Jason-3, SARAL/AltiKa, ICESat-2, Sentinel-3A, and Sentinel-3B; and Longyangxia (285 km²) from SARAL/AltiKa, CryoSat-2, ICESat-2, and Sentinel-3B.

3.3.2 Reservoir water area

Res-CN provides monthly reservoir area data derived from Landsat and Sentinel-2 images during 1984-2021. We compare these datasets with in situ water levels and altimetric measurements as well as other areal datasets (GRSAD and RealSAT). The 139 reservoirs with daily in-situ observations generally show good agreement in terms of reservoir area and in situ water level time series with 81% having CC values higher than 0.5. The CC value is expected to decrease for reservoirs with small areal sizes or steep banks. As an example, the CC values of Gutian and Hengjiang reservoirs (10 and 2 km^2) are 0.37 and 0.06, respectively. There is also a high median CC value of 0.70 in Res-CN water area against altimetric water level time series. As compared to HR altimetric water levels, approximately 63% of 244 compared reservoirs have good CC values exceeding 0.5, including 69 reservoirs with CC values > 0.8. For SR altimetric water levels, approximately 63% of compared 557 reservoirs have good CC values exceeding 0.5, among which 212 reservoirs show very good agreement with CC values > 0.8. Our cross validation was performed using two global data sources from RealSAT and GRSAD. RealSAT generated 681,137 monthly Lake-surface area maps from Landsat images during 1984-2015 using an ORBIT (Ordering-Based Information Transfer) approach that has been validated on 94 large reservoirs. As opposed to RealSAT, which generated new static lake polygons from water occurrence data, GRSAD used existing static surface water polygons, HydroLAKES and GRanD, to create monthly areas for 6,817 global reservoirs based on Landsat images over the last 35 years. To compare Res-CN with these two datasets, we spatially joined reservoir polygons from all datasets, identifying reservoirs with more than 90% overlap. The subset of reservoirs shows good agreement with GRSAD (Fig. 6a, median CC value of 0.65, rBIAS = -10%, rRMSE = 22%, n = 488) and RealSAT (Fig. 6b, median CC value = 0.64, rBIAS = -5%, rRMSE = 20%, n = 288). Since RealSAT and our collected in situ observations do not overlap, we validated only the GRSAD datasets against in situ water levels. GRSAD also showed a good agreement with CC values higher than 0.5 for 58% of 139 reservoirs, including 38 reservoirs that showed a very good agreement with CC values > 0.8. In sum, these comparisons suggest that our data set is reliable.
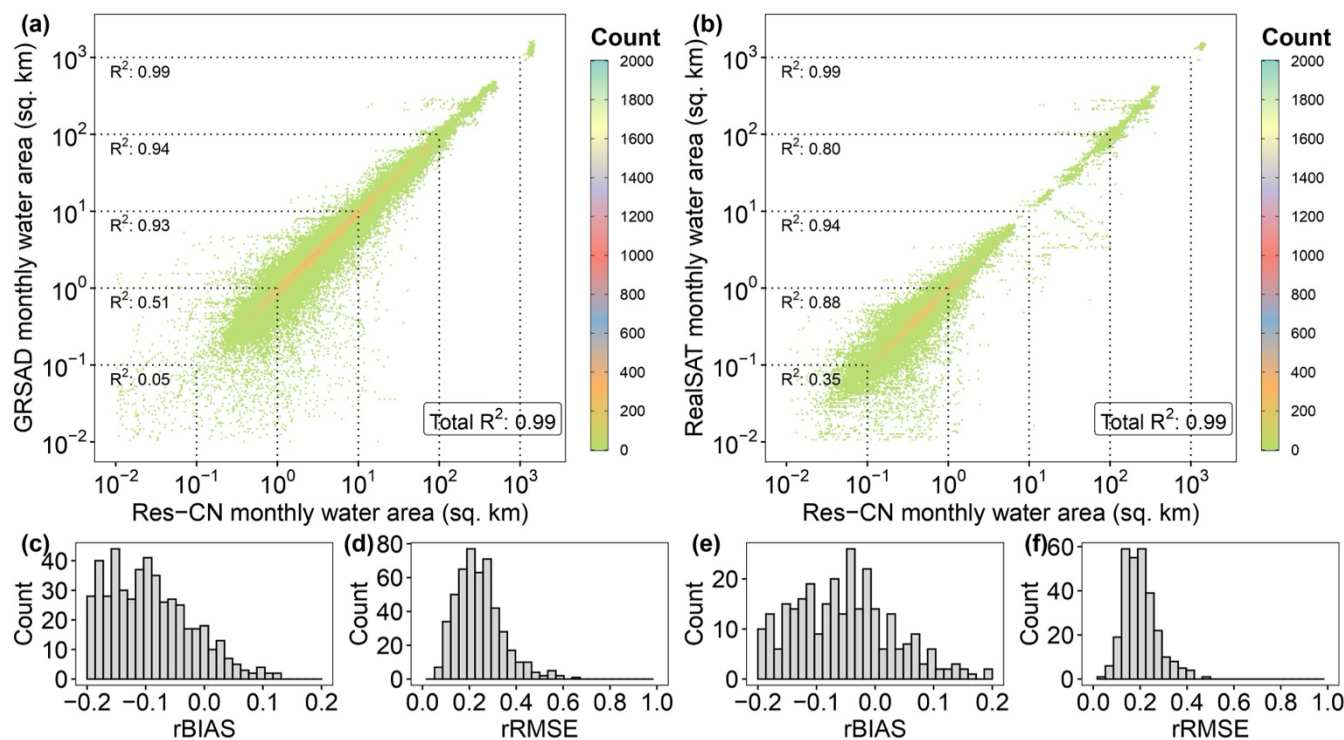
Figure 6. Cross validation of reconstructed monthly reservoir area values by comparing to two existing global datasets. (a, c, and d) Comparison between reconstructed monthly reservoir areas and GRSAD. (b, e, and f) Comparison between reconstructed monthly reservoir areas and RealSAT.

3.3.3 Reservoir storage variation

The Res-CN database provides monthly reservoir water storage variation for 3254 Chinese reservoirs during 1984-2020 using DEM's area-storage model. 74% reservoirs (89 of 119 validated reservoirs with in situ data) have good data quality with a RMSE value below 0.2 km^3 and a NRMSE value below 30%. NRMSE, CC, and RMSE have median values of 21%, 0.03 km^3 and 0.53 respectively. Lowest NRMSE is 7% in the Luhun reservoir, which has a high CC value of 0.90 and low RMSE value of 0.016 km^3. Figure 7 shows variations in water storage in small, medium, and large reservoirs located in different climate zones. The remotely sensed storage variations generally agree with the observations represented by the statistical metrics, although some large discrepancies occur in peak values. We find that our error statistics in terms of NRMSE are a bit higher than previous works in terms of NRMSE below 20% (Zhong et el., 2020). The errors result from the inaccuracy of the area-storage model developed by DEM as well as the error of water areas at certain reservoirs. To solve this problem, we provide another type of storage variation estimates using satellite water areas and water levels (see section 2.3, Shen et al., 2022b). Thea accuracy of storage variations is improved, with the median statistics of CC, NRMSE, and RMSE of 0.89, 11%, and 0.021 km^3, respectively.
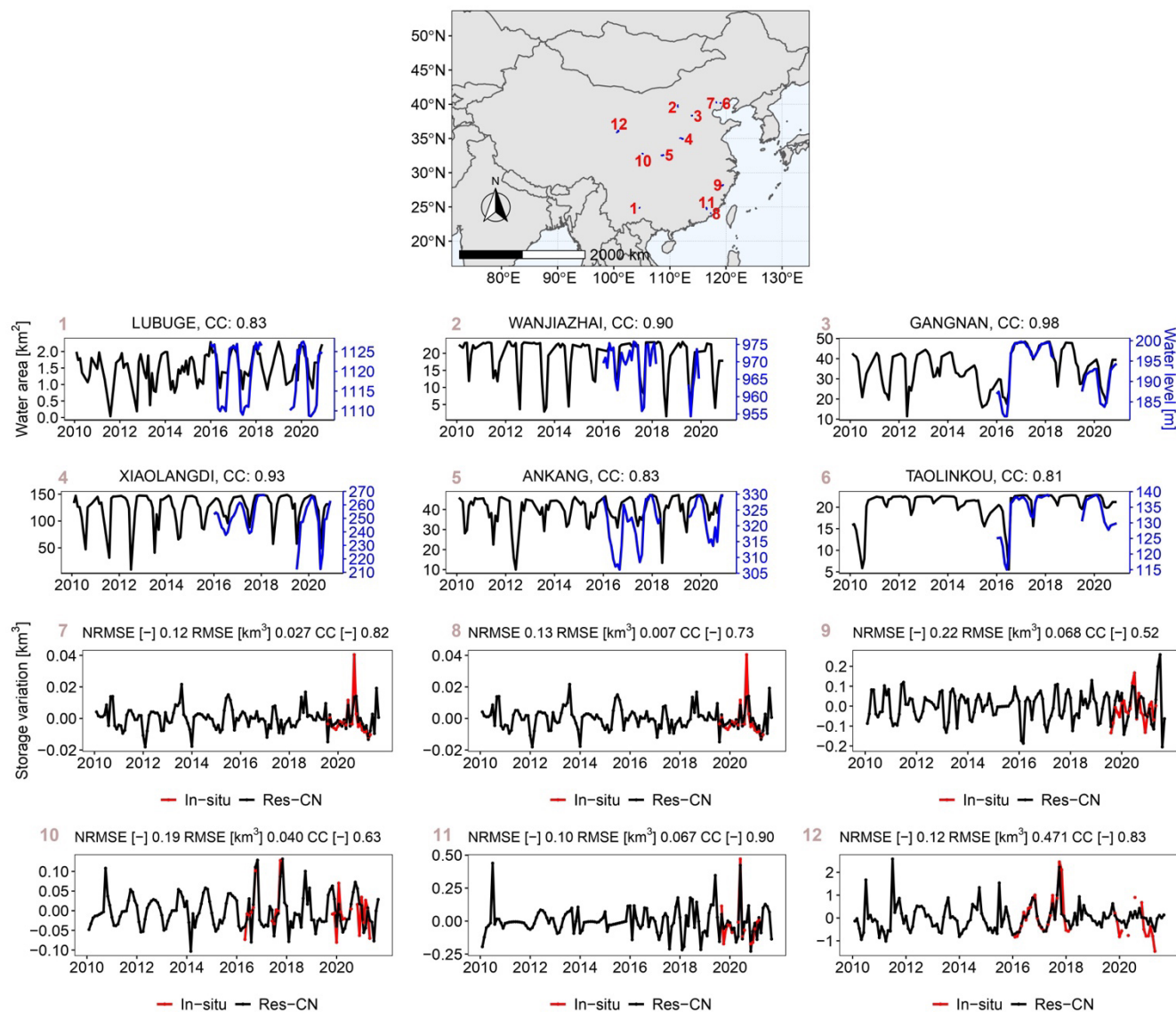
Figure 7. Time series of water area and storage variation in selected reservoirs. RMSE (km³), NRMSE, and CC values are given at the top of each subplot when in situ observations available. Note that: time series of water area and storage variation of the remaining reservoirs are available in our datasets.

3.3.4 Reservoir evaporation

Res-CN provides monthly reservoir evaporation values for 3254 Chinese reservoirs during 1984-2021. To assess the performance of the algorithm, one reservoir with observed pan evaporation is used here to demonstrate the reliability of the remotely sensed evaporation results (Fig. 8). Detailed validations of the algorithm can be found in Zhao et al. (2019; 2022). In general, the simulated results follow the observed pan evaporation well with a CC value of 0.57 and

relative bias value of -22%. The relatively low CC value is attributed to the fact that pan evaporation does not consider heat storage effects. By assuming the heat storage to be zero in the Penman Equation (Eq. (3)), the CC and relative bias

405   values are 0.65 and -15%. Meanwhile, there are clear differences and time lags between the pan evaporations and simulated results considering heat storage. By incorporating the heat storage into the simulation, more reliable reservoir evaporations are obtained from the remote sensing dataset. The long-term mean evaporation rates and water areas are also shown in Fig. 8. Reservoirs located in the southern and coastal areas have significantly larger values than other areas due to larger radiation values. For example, the mean evaporation for 613 reservoirs in Pearl River basin

410   is 1,210 mm/year, while the mean evaporation for 26 reservoirs in Songhua River basin is 717 mm/year. With respect to the mean reservoir areas (Fig. 8b), small and medium reservoirs are widely distributed across the nation. Long-term mean meteorological variables calculated the evaporation rates are available in Fig. S9. The CC values between the mean evaporation rates and the surface shortwave radiation, vapor pressure deficit, mean air temperature, and wind speed are 0.88, 0.84, 0.86, and 0.88, respectively.

415   Despite the good performance of the algorithm, some limitations are worth noting. Uncertainties in the evaporation estimates are generally attributed to three major sources, i.e., the input meteorological forcings, area estimations from Landsat images, and the limitations of the algorithms. As reported by Zhao et al. (2022), the uncertainty of reanalysis datasets is 7.22%, and the TerraClimate datasets used in this study produce the most reliable evaporation estimates, resulting in a total uncertainty value of 9.93%. Regarding reservoir water surface area, after applying the algorithm

420   developed by Donchyts et al. (2022), these impacts can be reduced to a large extent. There is some room for improving evaporation rate calculation, such as considering the effects of stratification on water temperature or including the advective heat fluxes from reservoir inflow, outflow, and groundwater.
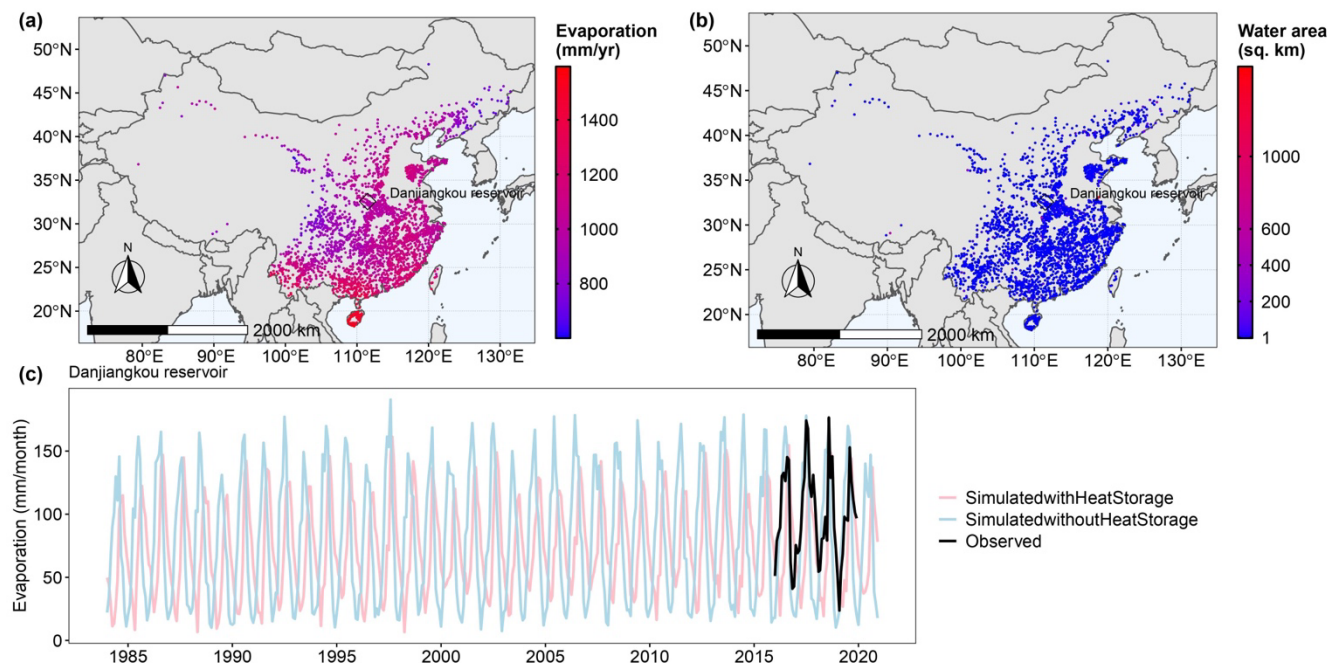
Figure 8. Validation of reconstructed monthly reservoir evaporation values. (a and b) Long-term mean evaporation rates and water
425 areas during 1984-2020. (c) Comparison between constructed monthly reservoir areas and observed pan evaporation values at the
Danjiangkou reservoir.

3.4 Res-CN products for reservoir catchment-level characteristics

3.4.1 Topographic characteristics

18 topographic attributes are provided in Res-CN (Table S10). The catchment area, slope, and catchment-level
430 elevation (including mean, maximum, minimum, standard deviation, range, and median values) were calculated based
on MERIT Hydro and MERIT DEM (Yamazaki et al., 2017; 2019). Slope was calculated using the algorithm developed
by Horn (1981). Moreover, we determine 10 indices of catchment shapes and stream network as they are vital in runoff
generation and flood situations. Mvert_ang is defined as the angle between the longitudinal axis and the north direction,
while mvert_dist is a catchment's longitudinal axis distance. These two indices could determine the relative
435 precipitation trajectory in combination with wind speed. Elog_ratio is a measure of roundness (i.e., the higher, the
rounder) of the catchment, and calculated according to Subramanya (2013). Strm_dens is often used for comparing
catchments as it is a function of many catchment attributes such as climate, soil, and geology. We used the MERIT-river
database to calculate stream density and length within a catchment. The form factor, shape factor, circulatory ratio,
relief of each catchment are also provided. Besides, we also added "resArearatio" to describe the proportion of the
440 reservoir area to the catchment area. High average catchment elevations and slopes are most apparent in the western

China, which extend from western Yunnan–Guizhou Plateau and southern Qinghai–Tibet Plateau to the northwestern areas (Fig. 9a and b). The streamflow density and resArearatio are relatively high in the central of the Yangtze River basin, where the artificial reservoirs are densely distributed (Fig. 9c and d). High elongation ratios are widespread in China and mvert_ang shows high values in the south (Fig. 9e and f).
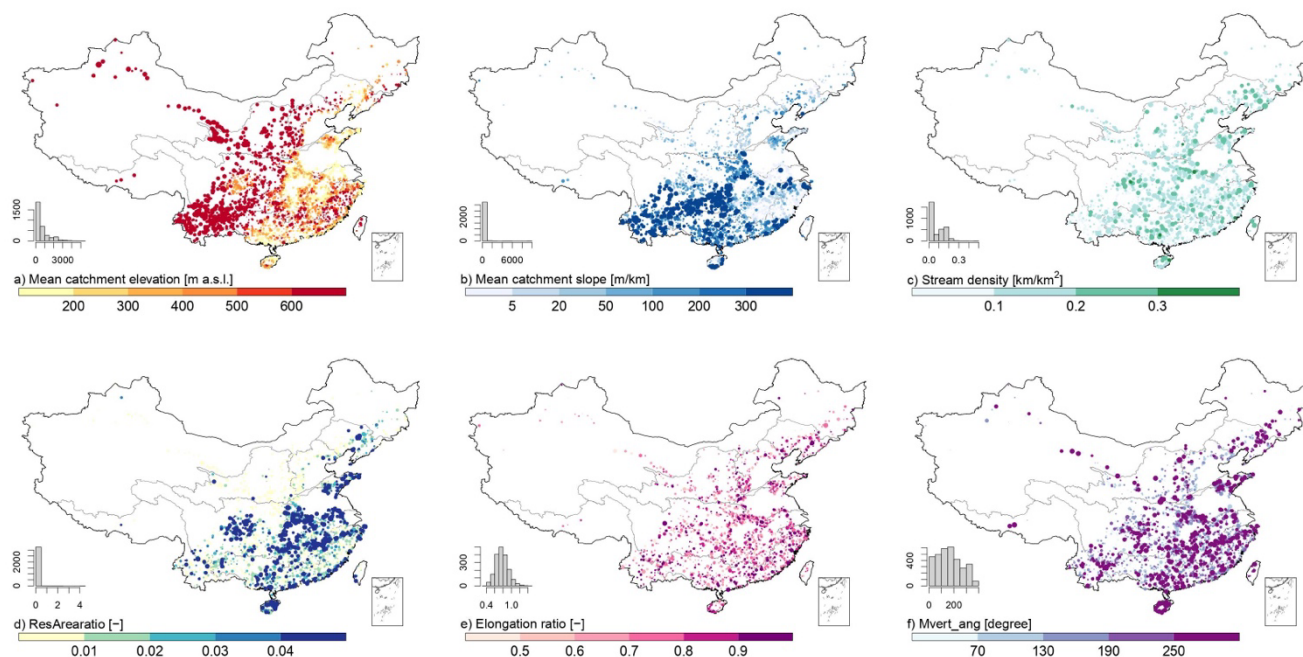
445

Figure 9. Distribution of selected topographic characteristics of intermediate catchments and full catchments. Each category's histogram indicates the number of basins (out of 3254). Circle sizes are proportional to catchment areas. In the figure caption, dimensionless is indicated by [-].

3.4.2 Climatic characteristics

450 Res-CN includes daily meteorological time series and 9 attributes reflecting aspects of climatic characteristics (Tables S11-12). In this study, we used the National Station-based Climatic Data set V3 (NSCD) to compute the catchment-level climatic characteristics at full catchments and intermediate catchments. NSCD provides daily meteorological time series during 1951–2020 and has near 800 stations in China, with the longest period of gauged observations of precipitation, temperature, evaporation, wind speed, pressure, sunshine duration, relative humidity, and near surface

455 temperature. The ground sites were sparse before 1970 (Hao et al., 2021). To ensure data quality and match the periods of other datasets in Res-CN, we used the latter 41 years (from 1980 to 2020) to generate a gridded data set based on the inverse distance weighting interpolation technique (Fig. A6). Figure 10 shows the spatial distribution of selected long-term mean meteorological forcings of full catchments and intermediate catchments. The precipitation, and mean air temperature have an increasing trend from northwest to southeast. The sunshine durations are high in the northern

460   areas where latitude is high, and the maximum value is 8.7 hour/day. Wind speed is generally high in the northern mountainous areas, southwestern, and coastal parts. The average evaporation is positively correlated with sunshine duration and is higher in Yellow River basin and southwest parts.

We calculated nine attributes for NSCD based on meteorological data between 1 October 1990 and 30 September 2018 to reflect aspects of climatic characteristics. Using the Global Aridity Index and Potential Evapotranspiration Climate
465   Database version 3(Zomer and Trabucco, 2022), we derived the reference evapotranspiration (ET_0) and aridity index. Aridity is often calculated as a function of precipitation, temperature and ET_0, and quantifies the precipitation availability for atmospheric water demand. Long-term daily precipitation, reference evapotranspiration, and aridity index (Fig. 10f) characterize the long-term climatic characteristics. The seasonality of precipitation (Fig. 10g) and the fraction of precipitation falling as snow (not shown) are two attributes characterizing seasonality, which yield the
470   yearly maps of sinusoidal precipitation cycle. Short-term events (e.g., heavy rainfall and drought) are characterized by the frequency and duration of heavy precipitation/dry days, and their most likely seasons of occurrence (Fig. 10h, i). High precipitation is most likely to occur in summer (Fig, 10h) for 86 % of all 3254 catchments, whereas dry days usually occur in winter (Fig, 10i) for 56 % of them.

One key limitation of the NSCD is that these gauged stations are unevenly distributed across the nation, and densely
475   grouped in the eastern and middle parts, which may affect the accuracy for some catchments. Nevertheless, the NSCD meteorological dataset has been widely used as the most reliable observational reference by many studies (Gu et al., 2022). It is produced from a larger number of gauged stations and followed by strict quality-assurance procedures and consistence-check. Its accuracy and completeness of each meteorological variable from 1951 to 2020 are significantly improved compared with similar data products in China, the missing rate of data of each element is generally below
480   1%, and the correct rate of data is close to 100%. Relative humidity suspicious rate 0.6%, large evaporation suspicious rate 1.2%, great wind suspicious rate 1.6%, the suspicious rate of other elements does not exceed one thousandth (Hao et al., 2021). The error rate of sunshine hours is one ten thousandth, and there is no wrong data for other meteorological variables.
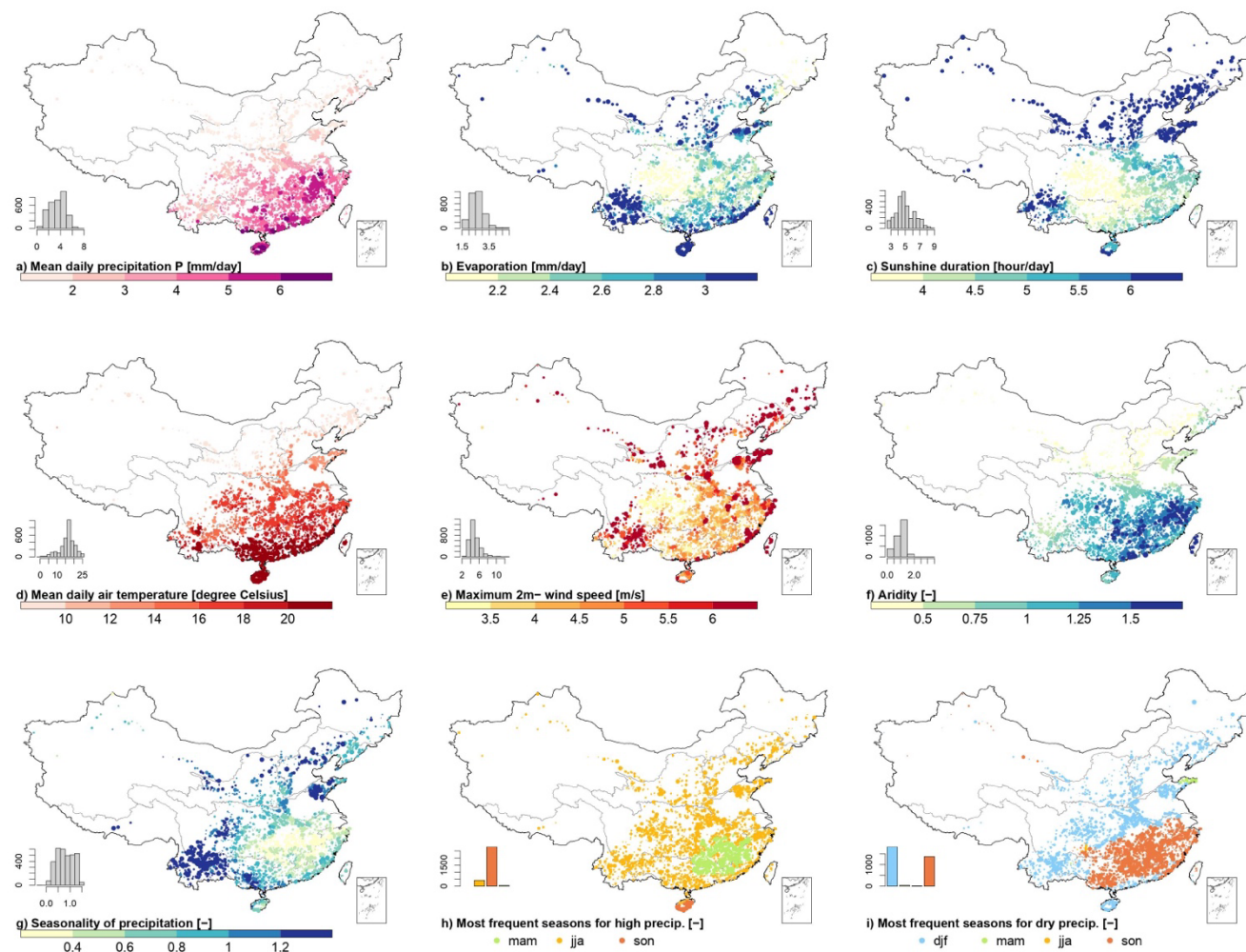
Figure 10. Distribution of selected long-term mean meteorological variables and climate indices of intermediate catchments and full catchments. Each category's histogram indicates the number of basins (out of 3254). Circle sizes are proportional to catchment areas. In the figure caption, dimensionless is indicated by [-].

3.4.3 Land cover characteristics

We provide three vegetation indices (EVI, enhanced vegetation index; LAI, leaf area index; NDVI, normalized difference vegetation index), two indicators of land use (GPP, gross primary productivity; NPP, net primary production), two average rooting depths (50 % and 90 %), and 10 land cover classes in each catchment (Table S13). LAI was derived from the MODIS MCD15A3H dataset with a temporal resolution of 4 days and a spatial resolution of 500 m (Myneni et al., 2015) and used for characterizing vegetation growth. NDVI and EVI were derived from the MODIS MOD13Q1 (Didan, 2021) and used to monitor and classify vegetation. These vegetation indices were computed as the maximum, minimum, or difference (e.g., LAI_{max}, LAI_{min}, and LAI_{diff}). LAI_{max} measures the maximum evaporative and vegetation interception

capacity, and LAI$_{diff}$ shows its temporal variations. GPP and NPP were derived from MODIS MOD17A2H (Running et al., 2021a) and MOD17A3HGF (Running et al., 2021b) dataset, respectively, and calculated for the whole period of 1 February 2000 to 1 January 2022. Meanwhile, the time series of both vegetation indices and indicators of land use are also provided in the Res-CN. Rooting depths are important parameters to characterize the water holding capacity

500 underground and annual evapotranspiration of topsoil. We calculated two average rooting depths (i.e., 50 % and 90 %) based on the IGBP (International geosphere–biosphere programme) classification (Zeng 2001).

Each catchment was described using 10 land cover classes based on ESA WorldCover 10 m (Zanaga et al., 2021). This dataset is a new baseline of global land cover product at 10 m spatial resolution for 2020 in almost near-real time based on both Sentinel-1 and Sentinel-2 data. Sentinel-1 can provide complimentary information on the observed structural

505 characteristics of land cover in areas where the Sentinel-2 images were covered by clouds. Thus, the combination of Sentinel-1 and Sentinel-2 data enables mapping land cover almost in real time. It includes 11 land cover classes and an overall accuracy of 75%, providing valuable information for food security, carbon assessment, biodiversity, and climate modelling. The dominant class and fractions of each class were computed at the GEE platform.

Some limitations of these datasets are identified. First, misclassification of ESA WorldCover occurs in areas of irrigated

510 agriculture and wetlands due to the high similarity of their hyperspectral spectrum. Second, although Res-CN provide time series of vegetation indices, it should be noted that NDVI often provides inaccurate measurements of vegetation density, the accuracy of which can only be guaranteed by long-term measurements. In addition, NDVI cannot provide quantitative estimates of vegetation density, so other attributes (i.e., LAI) are provided as a complement.

Trees are prevalent across the nation, and grasslands and croplands are another two dominant land cover in China.

515 Grassland has higher coverage largely in the Hai River Basin and the Yellow River Basin (Fig. 11c). Croplands are widespread in China, especially in the Yellow River, Yangtze River, and Huai River basins with a low mean slope (Fig. 11d). Fraction of barren sparse vegetation is quite small across the nation (Fig. 11e). Natural wetlands or water bodies are mainly distributed in the Yangtze River Basin and areas surrounding the Bo seas, and these water bodies are mainly artificial reservoirs and natural lakes (Fig. 11f). Catchments with a relatively high faction of snow and ice are mainly

520 located in the Tibet plateau, the source region of large rivers in China (not shown). A small proportion of the catchment area is typically considered as "built-up", and 6% of the catchments have impervious area greater than 0.05 (not shown). There is a spatial correlation between LAI$_{max}$ and LAI$_{diff}$ with trees fraction (CC = 0.74 and CC = 0.60, respectively). LAI$_{diff}$ has values similar to LAI$_{max}$ over most areas but should be smaller in areas with a high proportion of trees due to permanent green cover. Negative correlation is evident between the NDVI$_{max}$ (Fig. 11i, CC = −0.78) and the mean

525 catchment elevation (Fig. 9c).
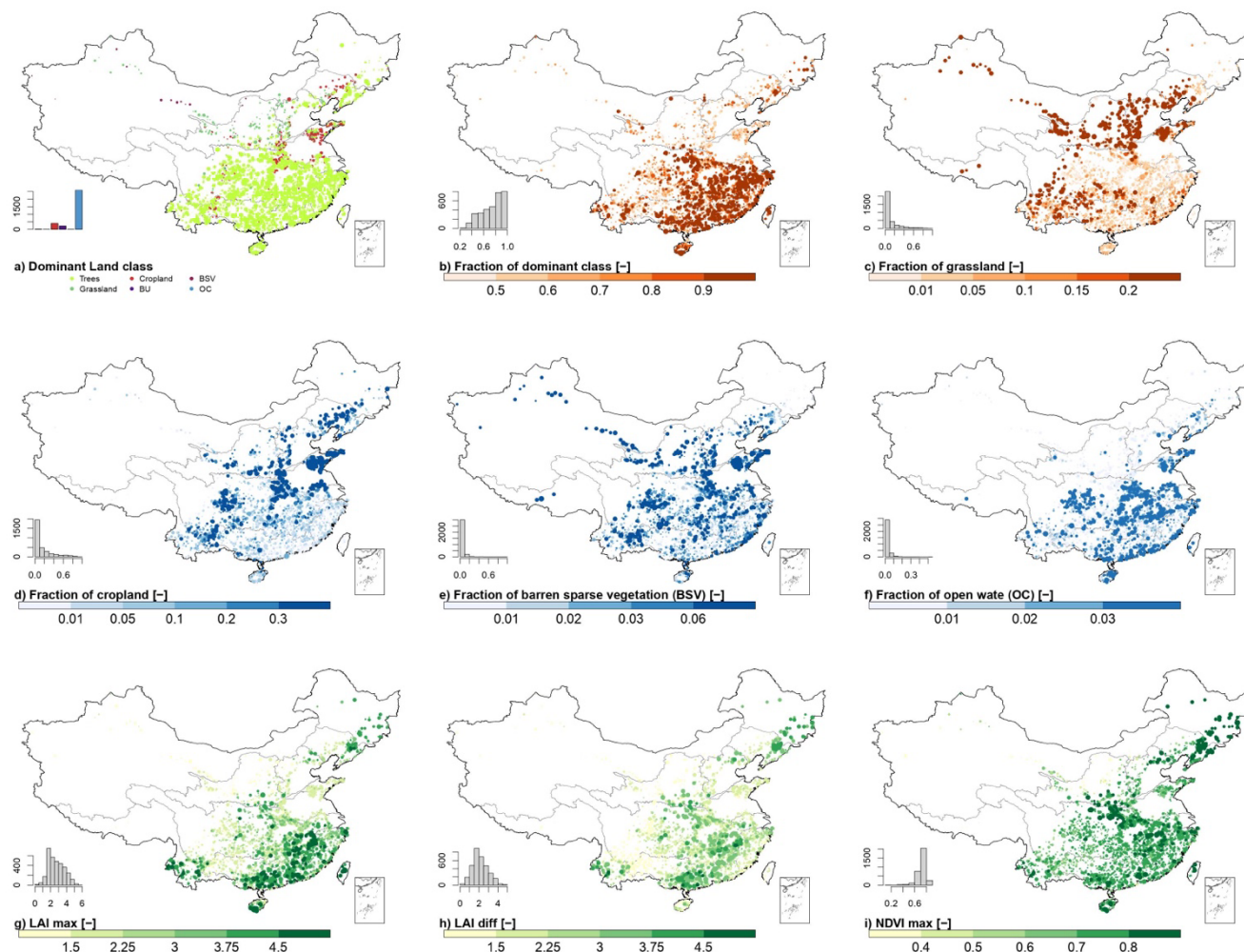
Figure 11. Distribution of selected land cover characteristics of intermediate catchments and full catchments. Each category's histogram indicates the number of basins (out of 3254). Circle sizes are proportional to catchment areas. In the figure caption, dimensionless is indicated by [-].

530 3.4.4 Soil & geology characteristics

Res-CN provided twenty attributes to characterize physical and chemical properties of soil (Tables S14). The pH in H_2O, cation exchange capacity (CEC), bulk density, and organic carbon content were determined from the SoilGrids250m dataset (SG250, Hengl et al., 2017). Machine learning methods were used to predict soil properties at six soil layers (i.e., 0–0.05 m, 0.05–0.15 m, 0.15–0.3 m, 0.3–0.6 m, 0.6–1 m, and 1–2 m) based on global observations from about 150,000

535 soil profiles and 158 environmental covariates from remote sensing data. Data within Res-CN are provided for each soil layer and all soil layers using depth-weighted averaging method. Soil pH is an important variable as it controls many other soil biological, chemical, and physical properties. CEC defines the sum of exchangeable cations that soil can

hold and is therefore a measure of fertility nutrient retention capacity. The density and organic carbon content refer to the mass of organic carbon per unit volume and mass, respectively. Besides SG250, the dataset of soil hydraulic and
540   thermal parameters produced by Dai et al. (2019) was also used. Dai et al. (2019) generated six soil layers of global soil hydraulic and thermal parameters with four products of vertical profiles available using multiple PTFs (Pedotransfer Functions) based on SG250 and soil dataset from Shangguan et al. (2014). We adopted the products with the vertical resolutions of SG250 and computed soil characteristics (saturated water content, saturated hydraulic conductivity, and other thermal parameters) for all soil layers. Additional attributes derived from Shangguan et al. (2013) include clay,
545   silt, sand, and rock fragment proportions, soil profile depth, and soil organic carbon content (SOC). With the use of the polygon linkage method, this database provides soil physical and chemical attributes for land surface modeling in China at a 30 arcsec resolution. Proportions of clay, silt, sand refer to the fractions of the particles < 0.002 mm, particles ≥ 0.002 mm and ≤ 0.05 mm, and particles > 0.05 mm and < 2 mm in the fraction of particles smaller than 2 mm, respectively. SOC is a key variable for ecosystems and affects moisture regimes and ground thermal.

550   Geology characteristics are described by 19 attributes (i.e., subsurface porosity, permeability, and lithological classes) derived from global lithological map (GliM, Hartmann and Moosdorf, 2012) and global hydrogeology maps, (GLHYMPS, Gleeson et al., 2014) datasets (Table S15). The two important parameters for ground water modeling, subsurface porosity and permeability, came from the GLHYMPS. Subsurface porosity is a measure of the ability of the subsurface to store water, while permeability is a measure of the ability of the rock to transmit fluids. Both these two parameters
555   show a high spatial correlation with GliM map, as hydraulic properties in GLHYMPS are based primarily on lithological classes of GLiM. We computed the catchment-level characteristics by applying an arithmetic mean method for porosity and arithmic scale geometric mean method for permeability. The lithological classes were derived from the GliM, which was created by summarizing 92 regional lithological maps and offers three classification levels of detail. In this study, we adopted the first level of GLiM, that has 16 lithological classes. Proportions of each lithological class and the
560   dominant class are documented in our datasets.

There are some limitations with these datasets. Firstly, The GLHYMPS module is primarily useful for analyzing regional scales, i.e., scales larger than 5 km, where the effects of local heterogeneities such as fault zones are negligible (Gleeson et al., 2014). Secondly, GLHYMPS is not adequate for analysis at regions dominated by unsaturated processes such as deeply weathered soils, as it is modeled for saturated conditions (Huscroft et al., 2018). Thirdly, data quality varies
565   depending on location, based on raw regional geological maps available in different resolutions and data quality. In this study, the resolution of the Chinese raw data sources is slightly lower than that of GLiM (Hao et al., 2021).

The soil pH value is high in the northern and northeastern China, and the saturated water content is low in this area (Fig. 12a and b). High values of CEC can be found in central and northeastern China and forested parts on the Qinghai– Tibet Plateau (Fig. 12c). The clay content is low in the northern China, while the sand content shows the opposite
570   pattern (Fig. 12d and e). The silt content has a wide predominance pattern in China, particularly in the middle and

northeastern parts (Fig. 12f). Moreover, we found that soil characteristics are correlated with other attributes from Res-CN as they are predicted by fusing multisource covariates such as climate and landscape attributes. For example, the soil texture (i.e., sand, silt, and clay contents) shows similar pattern of the aridity index (Fig. 12e and Fig. 10f). SOC has a high correlation value with surface slope (Fig. 12c and Fig. 10b, R^2 = 0.94). The geology attributes have a clear

575 latitude distribution, and the main lithological classes include acid plutonic rocks (21% of the catchments), siliciclastic sedimentary (20%), mixed sedimentary (19%), and carbonate sedimentary (17%). Medium subsurface porosity and high permeability are typically in north and coastal surrounding the Bohai Sea areas with abundant unconsolidated sediments, and high porosity and low permeability are often associated with mixed sedimentary rocks in northern Inner Mongolia, western Yunnan–Guizhou Plateau and southern Qinghai–Tibet Plateau (Fig. 12h, i, and e). Interestingly,

580 high values of subsurface porosity are not necessarily accompanied by high values of permeability, producing a more heterogeneous spatial pattern (Fig. 12h) than that in Fig. 12i. There may be differences in permeability and porosity due to the different rock structures of GLiM (Gleeson et al., 2014).
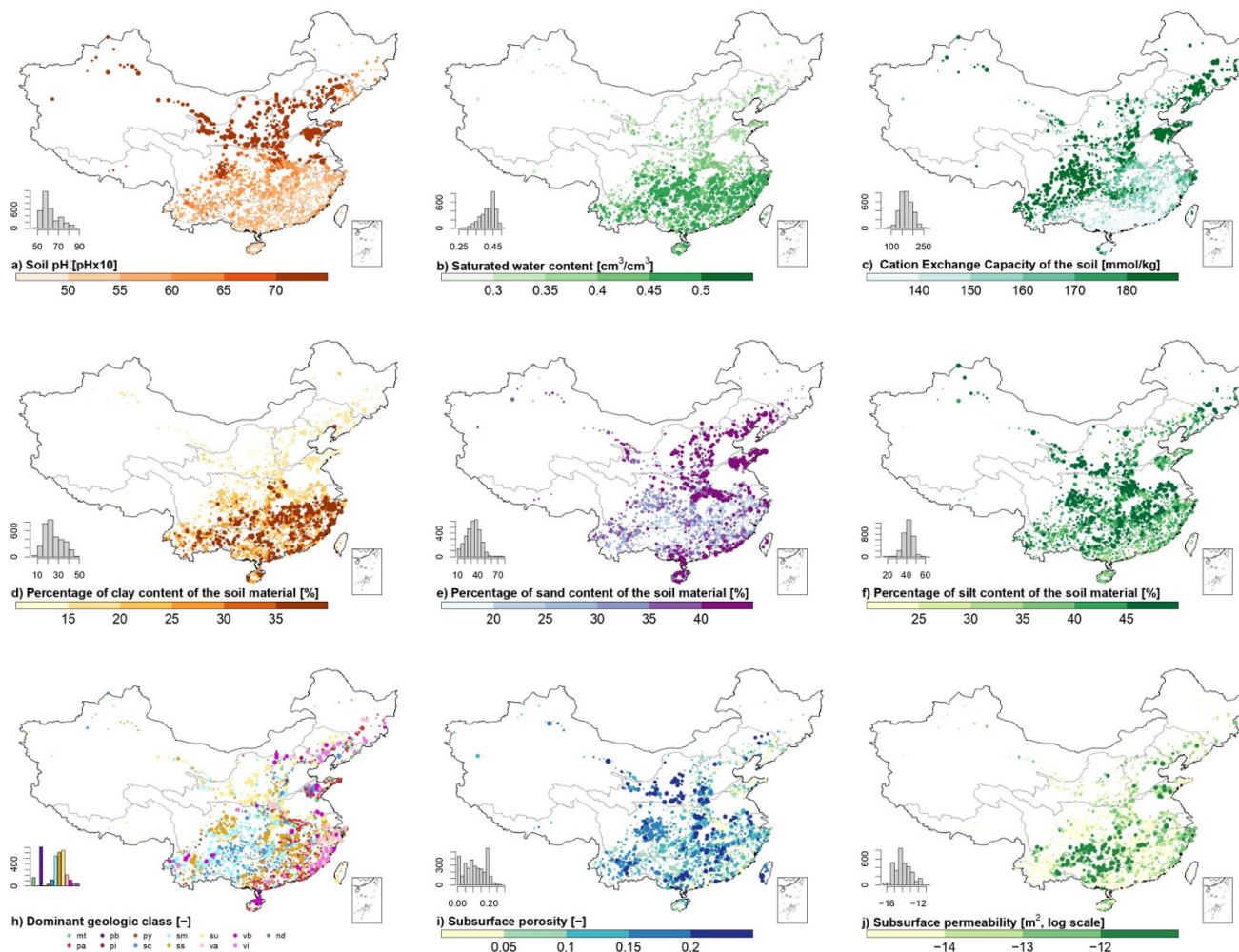
Figure 12. Distribution of selected soil and geology characteristics of intermediate catchments and full catchments. Each category's histogram indicates the number of basins (out of 3254). Circle sizes are proportional to catchment areas. In the figure caption, dimensionless is indicated by [-].

3.4.5 Anthropogenic activity characteristics

We computed four indices of anthropogenic activities in the catchments, including population count, human footprint, nighttime lights, and road density (Table S16). Population counts were derived from the GPW v4.11 (Gridded population of the world, Center for International Earth Science Information Network – CIESIN - Columbia University, 2018). This collection produces human population estimates for five years (i.e., 2000, 2005, 2010, 2015, and 2020) at a gridded resolution of 30 arc-seconds. Human footprint is a measure of human activities that use natural resources on earth and was extracted from the Global Human Footprint dataset (Venter et al., 2016). This database measures the cumulative environmental impact of indirect and direct human activities in 1993 and 2009, and was produced by eight

595   inputs: electric infrastructure, population density, built environments, pastures, crop lands, roads, railroads, and navigable waterways. Nighttime lights are a measure of human activity intensity and were derived from the DMSP-OLS Nighttime Lights version 4 (Defense Meteorological Program-Operational Line-Scan, Doll, 2008). This database can detect visible and near-infrared emission sources at night and consists of cloud-free composites made using all the available archived DMSP-OLS smooth resolution data at a resolution of 30 arc-seconds. The "avg_lights_x_pc" in this

600   dataset is used in this study and represents the mean value of cloud-free light detections in the visible band. The road density was obtained from Global Roads Inventory Project (Meijer et al., 2018), providing global raster datasets of road density at a 5 arcminutes spatial resolution. Using 60 geospatial datasets on road infrastructure, this inventory gathers, harmonizes, and integrates over 21 million km of roads by country.

     These datasets are subject to some limitations. First, cumulative pressures of human footprint are static through time

605   due to a lack of available data, which would lead to an underestimation of human footprint if those pressures expanded at an above-average rate. Second, some static pressures, like the pollution and invasive species are not considered in the cumulative pressures of human footprint. Third, the GRIP datasets cannot quantify historic road expansion due to the missing information on the year of construction. Fourth, DMSP-OLS has the blooming effect (i.e., overestimation of lit area) due to the low spatial resolution and the reflectance of light from adjacent water bodies.

610   Figure 13 illustrates the spatial distribution of four anthropogenic indices in the catchments. Road density, population count, lights, and human footprint show the similar patterns, suggesting that intense human activities are distributed in the coastal lines surrounding the East and Bo seas, middle, and northeastern China and there is almost no human activity in the northwestern China due to high elevation and harsh environment.
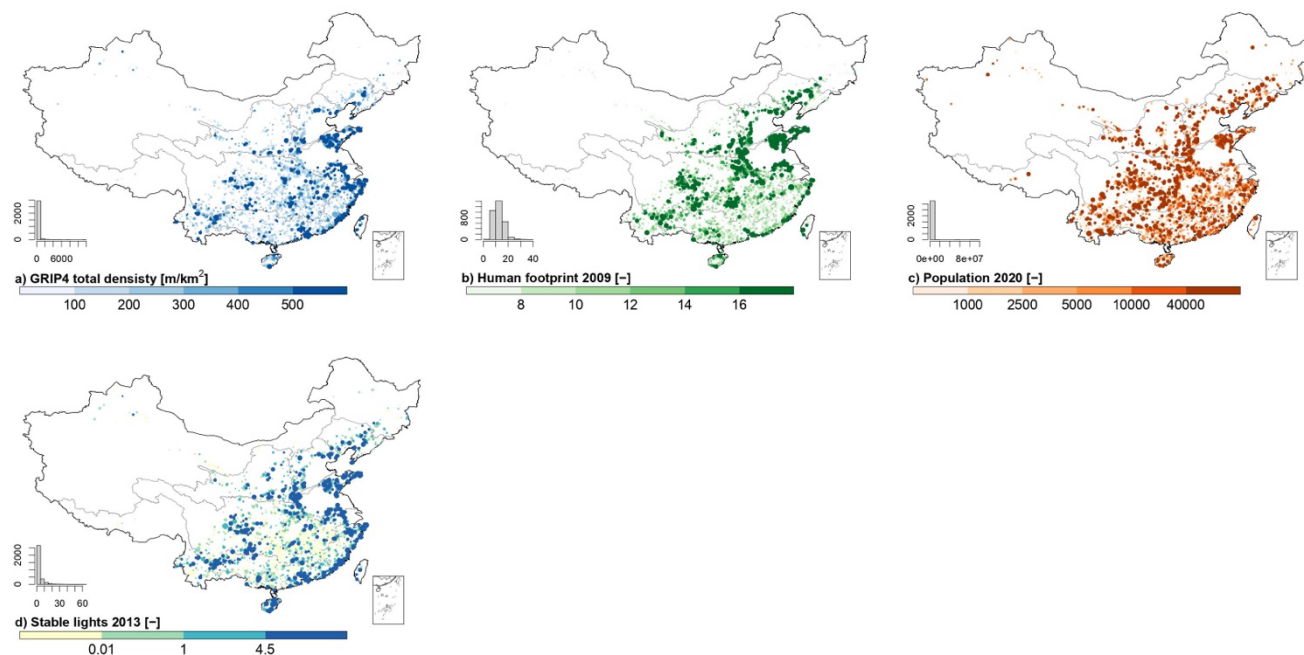
Figure 13. Distribution of human activity characteristics of intermediate and full catchments. Each category's histogram indicates the number of basins (out of 3254). Circle sizes are proportional to catchment areas. In the figure caption, dimensionless is indicated by [-].

4 Data availability

Res-CN archive can be found here https://doi.org/10.5281/zenodo.7390715 (Shen et al., 2022a). They are distributed with a CC-BY license. The files provided are (A) shapefiles, (B) full catchments containing all catchment-level attributes such as climate, topographic, land cover, soil, geological, anthropogenic activities, and time series of meteorological variables, (C) intermediate catchments, (D) reservoir states (i.e., water level, area, evaporation, and storage variation) and (E) info English file containing more information of RES-CN. All input datasets are summarized in the supplements and kindly acknowledged.

5 Summary and applications

In this study, we have produced a comprehensive and extensive data of reservoir-catchment characteristics in China, Res-CN, which complementarily improved the existing reservoir datasets. We demonstrated that the construction of Res-CN involved a first known effort to construct catchment-level characteristics of reservoirs for our delineated full catchments and intermediate catchments of reservoirs. These two types of catchments allow investigations within individual catchments (full catchment) and interconnected river networks. In total, we provided 512 static catchment-

level attributes for 3254 reservoirs in six categories (i.e., reservoir catchment, topography, climate, soil and geology, land cover and use, and anthropogenic activity). Additionally, 15 climatic variables were extracted at daily scale, which can drive machine learning models or hydrological models for simulations. Alongside the catchment-level attributes, we produced a significantly enhanced spatial and temporal coverage (e.g., 67% increase in spatial resolution of water

635 level and 225% increase in storage anomaly) of water level (data available for 20% of 3,254 reservoirs), water area (99%), storage anomaly (92%), and evaporation (98%) by utilizing multiple satellites such as operational satellite altimeters and imagery data. In situ data of 138 reservoirs are employed in this study as a valuable reference for evaluation, thus enhancing our confidence in the data quality and enhancing our understanding of accuracy of current satellite datasets. We have considered and discussed the deficits, limitations, and uncertainties of Res-CN for further

640 applications.

We envision that Re-CN with its comprehensive and extensive attributes can provide strong supports to a wide range of applications and disciplines. Firstly, the included catchment-level attributes and time series with a high temporal resolution as well as the interconnected stream network offer exciting opportunities in a spatially explicit context to simulate the water and sediment transfer if appropriate approaches are used. For example, machine-learning methods

645 make it possible to predict reservoir storage change at 1- to 3-month lead from reservoir upstream attributes and time-series of reservoir states (Tiwari et al., 2019). Secondly, Res-CN provide thus far the most comprehensive reservoir states in China for assessing impacts of reservoir regulation and dynamics. Tracking the spatiotemporal balance of reservoir evaporative and water storage can provide a basis for local water management in a warming climate (Di Baldassarre et al., 2019). The reservoir operational rules or impacts of reservoir regulation on flow regimes are

650 possibly to be inferred from reservoir water dynamics in Res-CN (Vu et al., 2022). This is particularly true if the reservoir inflow is also utilized. Recently, the gridded natural runoff provided by Gou et al. (2021) provides exciting opportunities for quantifying the human water regulation in combination with Res-CN. Thirdly, catchment-level attributes are important and can be used to explore water fluxes and sediment transportation especially in reservoirs that have not been sampled. Studies on cascading patterns in reservoir attributes found that each attribute may display

655 linear function of catchment area, concluding that cascading patterns of each attribute have different implications for dam management (Faucheux et al., 2022). For instance, one study combined knowledge of basin attributes with economic, climate, and landscape data to inform reservoir removal decisions in California's Central Valley basin (Null et al., 2014). Besides, these catchment-level attribute datasets have also been demonstrated to be highly valuable in other studies (Addor et al., 2017; Coxon et al., 2020). Lastly, carbon dioxide emissions from reservoirs show significant

660 spatial and seasonal variation, highlighting the importance of hydrology in terrestrial–reservoir carbon transfers and the need to consider this effect when plumbing terrestrial carbon budgets. Res-CN also offers exciting opportunities to address changes in reservoir storage that may be linked to carbon dioxide emissions changes.

6 Code availability

All scripts for generating our reservoir datasets are publicly available (Once the paper accepted, it would be uploaded
665   at the same DOI of Res-CN). A copy of all scripts is available for peer reviewers upon request.

Supplements.

Supplement contains many Tables, Figures, and Texts illustrating the methodologies and source datasets for generating
the Res-CN, as well as detailed evaluations of our Res-CN datasets and all necessary explanations related to this article.

Author contributions.

670   Y.S. and D.Y. designed the research and initiated the investigation. Y.S. processed the datasets and created the figures.
K.N. extracted data from satellite altimeters. Y.S. wrote and prepared the manuscript with suggestions from co-authors.

Competing interests.

The authors declare that they have no conflict of interest.

Acknowledgements.

675   Data from various data centers were acknowledged by the authors. For more acknowledgements, please refer to our
supplementary and our datasets. Youjiang Shen also acknowledge the contributions from the EOForChina project.

Financial supports.

This study was financially supported by the funding JSPS KAKENHI 21H05002. The first author is supported by the
China Scholarship Council.

680 **Appendix.**
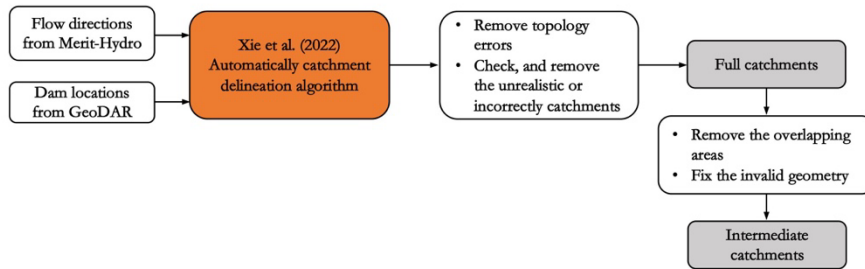
Figure A1. Flowchart of the algorithm for generating reservoir upstream catchments.
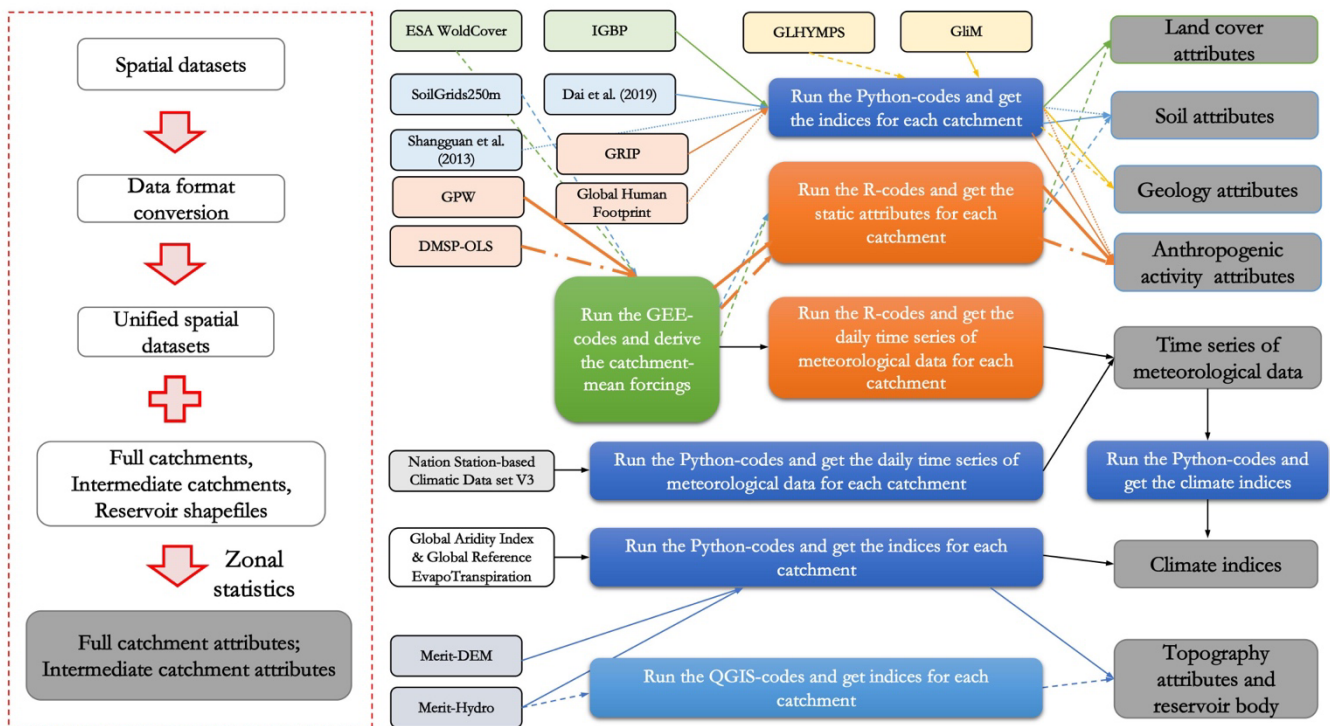
Figure A2. Flowchart for generating reservoir upstream catchment-level characteristics. (Overview of the methodology at the left
685 panel, we give the detailed steps for generating each attribute based on our provided codes. Users can freely access our codes in our
Res-CN product.

References

Busker, T., de Roo, A., Gelati, E., Schwatke, C., Adamovic, M., Bisselink, B., Pekel, J.-F., and Cottam, A.: A global lake and reservoir volume analysis using a surface water dataset and satellite altimetry, Hydrol. Earth Syst. Sci., 23, 690   669–690, https://doi.org/10.5194/hess-23-669-2019, 2019.

Chaudhari, S., Felfelani, F., Shin, S., and Pokhrel, Y.: Climate and anthropogenic contributions to the desiccation of the second largest saline lake in the twentieth century, J. Hydrol., 560, 342–353, https://doi.org/10.1016/j.jhydrol.2018.03.034, 2018.

Marx, A., Dusek, J., Jankovec, J., Sanda, M., Vogel, T., van Geldern, R., Hartmann, J., and Barth, J. A. C.: A review of CO2 and 695   associated carbon dynamics in headwater streams: A global perspective, Rev. Geophys., 55, 560–585, https://doi.org/10.1002/2016RG000547, 2017.

Buccola, N. L., Risley, J. C., and Rounds, S. A.: Simulating future water temperatures in the north Santiam River, Oregon, J. Hydrol., 535, 318–330, https://doi.org/10.1016/j.jhydrol.2016.01.062, 2016.

Boulange, J., Hanasaki, N., Yamazaki, D., Pokhrel, Y.: Role of dams in reducing global flood exposure under climate 700   change, Nat. Commun., 12, 1–7, https://doi.org/10.1038/s41467-020-20704-0, 2021.

Li, R., Xiong, L., Xiong, B., Li, Y., Xu, Q., Cheng, L., and Xu, C.-Y.: Investigating the downstream sediment load change by an index coupling effective rainfall information with reservoir sediment trapping capacity, J. Hydrol., 590, 125200, https://doi.org/10.1016/j.jhydrol.2020.125200, 2020.

Ngor, P. B., Legendre, P., Oberdorff, T., and Lek, S.: Flow alterations by dams shaped fish assemblage dynamics in the 705   complex Mekong-3S river system, Ecol. Indic., 88, 103–114, https://doi.org/10.1016/j.ecolind.2018.01.023, 2018.

Crétaux, J.-F., Jelinski, W., Calmant, S., Kouraev, A., Vuglinski, V., Bergé-Nguyen, M., Gennero, M.-C., Nino, F., Del Rio, R. A., Cazenave, A., and Maisongrande, P.: SOLS: a lake database to monitor in the Near Real Time water level and storage variations from remote sensing data, Adv. Space Res., 47, 1497–1507, 710   https://doi.org/10.1016/j.asr.2011.01.004, 2011.

Birkett, C., Reynolds, C., Beckley, B., and Doorn, B.: From research to operations: the USDA global reservoir and lake monitor, In: Coastal Altimetry. Springer, Berlin, Heidelberg, 19–50, https://doi.org/10.1007/978-3-642-12796-0_2, 2011.

Schwatke, C., Dettmering, D., Bosch, W., and Seitz, F.: DAHITI – an innovative approach for estimating water level time 715   series over inland waters using multi-mission satellite altimetry, Hydrol. Earth Syst. Sci., 19, 4345–4364, https://doi.org/10.5194/hess-19-4345-2015, 2015.

Markert, K. N., Pulla, S. T., Lee, H., Markert, A. M., Anderson, E. R., Okeowo, M. A., and Limaye, A. S.: AltEx: An open source web application and toolkit for accessing and exploring altimetry datasets, Environ. Modell. Softw., 117, 164–175, https://doi.org/10.1016/j.envsoft.2019.03.021, 2019.

720   Tourian, M. J., Elmi, O., Shafaghi, Y., Behnia, S., Saemian, P., Schlesinger, R., and Sneeuw, N.: HydroSat: geometric quantities of the global water cycle from geodetic satellites, Earth Syst. Sci. Data, 14, 2463–2486, https://doi.org/10.5194/essd-14-2463-2022, 2022.

Gao, H., Birkett, C., and Lettenmaier, D. P.: Global monitoring of large reservoir storage from satellite remote sensing, Water Resour. Res., 48, W09504, https://doi.org/10.1029/2012WR012063, 2012.

725   Tortini, R., Noujdina, N., Yeo, S., Ricko, M., Birkett, C. M., Khandelwal, A., Kumar, V., Marlier, M. E., and Lettenmaier, D. P.: Satellite-based remote sensing data set of global surface water storage change from 1992 to 2018, Earth Syst. Sci. Data, 12, 1141-1151, https://doi.org/10.5194/essd-12-1141-2020, 2020.

Shen, Y., Nielsen, K., Revel, M., Liu, D., and Yamazaki, D.: A dataset for reservoir-catchment characteristics for 3254 Chinese reservoirs, i.e., Res-CN [Data set]. Zenodo. https://doi.org/10.5281/zenodo.7390715, 2022a.

730   Shen, Y., Liu, D., Jiang, L., Nielsen, K., Yin, J., Liu, J., and Bauer-Gottwein, P.: High-resolution water level and storage variation datasets for 338 reservoirs in China during 2010–2021, Earth Syst. Sci. Data, 14, 5671–5694, https://doi.org/10.5194/essd-14-5671-2022, 2022b.

Pekel, J.-F., Cottam, A., Gorelick, N., and Belward, A. S.: High-resolution mapping of global surface water and its long-term changes, Nature, 540, 418–422, https://doi.org/10.1038/nature20584, 2016.

735   Zhao, G., and Gao, H.: Automatic Correction of Contaminated Images for Assessment of Reservoir Surface Area Dynamics, Geophys. Res. Letters, 45, 6092–6099, https://doi.org/10.1029/2018GL078343, 2018.

Khandelwal, A., Karpatne, A., Ravirathinam, P. Ghosh, R., Wei. Z., Dugan, H. A., Hanson, P. C., and Kumar, V.: ReaLSAT, a global dataset of reservoir and lake surface area variations, Sci. Data, 9, 356, https://doi.org/10.1038/s41597-022-01449-5, 2022.

740   Yao, F., Wang, J., Wang, C., and Crétaux, J.-F.: Constructing long-term high-frequency time series of global lake and reservoir areas using Landsat imagery, Remote Sens. Environ., 232, 111210, https://doi.org/10.1016/j.rse.2019.111210, 2019.

Liu, J., Jiang, L., Zhang, X., Druce, D., Kittel, C. M. M., Tøttrup, C., and Bauer-Gottwein, P.: Impacts of water resources management on land water storage in the North China Plain: Insights from multi-mission earth observations,
745   J. Hydrol., 603, 126933, https://doi.org/10.1016/j.jhydrol.2021.126933, 2021.

Donchyts, G., Winsemius, H., Baart, F., Dahm, R., Schellekens, J., Gorelick, N., Iceland, C., and Schmeier, S.: High-resolution surface water dynamics in Earth's small and medium-sized reservoirs, Sci. Rep., 12, 13776, https://doi.org/10.1038/s41598-022-17074-6, 2022.

Klein, I., Mayr, S., Gessner, U., Hirner, A., and Kuenzer, C.: Water and hydropower reservoirs: High temporal resolution
750   time series derived from MODIS data to characterize seasonality and variability, Remote Sens. Environ., 253, 112207, https://doi.org/10.1016/j.rse.2020.112207, 2021.

Hou, J., van Dijk, A. I. J. M., Beck, H. E., Renzullo, L. J., and Wada, Y.: Remotely sensed reservoir water storage dynamics (1984–2015) and the influence of climate variability and management at a global scale, Hydrol. Earth Syst. Sci., 26, 3785–3803, https://doi.org/10.5194/hess-26-3785-2022, 2022.

755 Vu, D. T., Dang, T. D., Galelli, S., and Hossain, F.: Satellite observations reveal 13 years of reservoir filling strategies, operating rules, and hydrological alterations in the Upper Mekong River basin, Hydrol. Earth Syst. Sci., 26, 2345–2364, https://doi.org/10.5194/hess-26-2345-2022, 2022.

Tian, W., Liu, X., Wang, K., Bai, P., Liu, C., and Liang, X.: Estimation of global reservoir evaporation losses, J. Hydrol., 607, 127524, https://doi.org/10.1016/j.jhydrol.2022.127524, 2022.

760 Zhao, G., and Gao, H.: Estimating reservoir evaporation losses for the United States: Fusing remote sensing and modeling approaches, Remote Sens. Environ., 226, 109-124, https://doi.org/10.1016/j.rse.2019.03.015, 2019.

Zhao, G., Li, Y., Zhou, L., and Gao, H.: Evaporative water loss of 1.42 million global lakes. Nat. Commun., 13, 3686, https://doi.org/10.1038/s41467-022-31125-6, 2022.

Lehner, B., Liermann, C. R., Revenga, C., Vörösmarty, C., Fekete, B., Crouzet, P., Döll, P., Endejan, M., Frenken, K., Magome, 765 J., Nilsson, C., Robertson, J. C., Rödel, R., Sindorf, N., and Wisseret, D.: High-resolution mapping of the world's reservoirs and dams for sustainable river-flow management, Front. Ecol. Environ., 9, 494–502, https://doi.org/10.1890/100125, 2011.

Messager, M. L., Lehner, B., Grill, G., Nedeva, I., and Schmitt, O.: Estimating the volume and age of water stored in global lakes using a geo-statistical approach, Nat. Commun., 7, 13603, https://doi.org/10.1038/ncomms13603, 2016.

770 Chen, T., Song, C., Fan, C. Cheng, J., Duan, X., Wang, L., Liu, K., Deng, S., and Che, Y.: A comprehensive data set of physical and human-dimensional attributes for China's lake basins. Sci. Data., 9, 519, https://doi.org/10.1038/s41597-022-01649-z, 2022.

Lehner, B., Messager, M. L., Korver, M. C. and Linke, S.: Global hydro-environmental lake characteristics at high spatial resolution. Sci. Data, 9, 351, https://doi.org/10.1038/s41597-022-01425-z, 2022.

775 Liu, J., Fang, P., Que, Y., Zhu, L.-J., Duan, Z., Tang, G., Liu, P., Ji, M., and Liu, Y.: A dataset of lake-catchment characteristics for the Tibetan Plateau, Earth Syst. Sci. Data, 14, 3791–3805, https://doi.org/10.5194/essd-14-3791-2022, 2022.

Addor, N., Newman, A. J., Mizukami, N., and Clark, M. P.: The CAMELS data set: catchment attributes and meteorology for large-sample studies, Hydrol. Earth Syst. Sci., 21, 5293–5313, https://doi.org/10.5194/hess-21-5293-2017, 780 2017.

Alvarez-Garreton, C., Mendoza, P. A., Boisier, J. P., Addor, N., Galleguillos, M., Zambrano-Bigiarini, M., Lara, A., Puelma, C., Cortes, G., Garreaud, R., McPhee, J., and Ayala, A.: The CAMELS-CL dataset: catchment attributes and meteorology for large sample studies – Chile dataset, Hydrol. Earth Syst. Sci., 22, 5817–5846, https://doi.org/10.5194/hess-22-5817-2018, 2018.

785   Chagas, V. B. P., Chaffe, P. L. B., Addor, N., Fan, F. M., Fleis- chmann, A. S., Paiva, R. C. D., and Siqueira, V. A.: CAMELS- BR: hydrometeorological time series and landscape attributes for 897 catchments in Brazil, Earth Syst. Sci. Data, 12, 2075–2096, https://doi.org/10.5194/essd-12-2075-2020, 2020.

Coxon, G., Addor, N., Bloomfield, J. P., Freer, J., Fry, M., Han- naford, J., Howden, N. J. K., Lane, R., Lewis, M., Robinson, E. L., Wagener, T., and Woods, R.: CAMELS-GB: hydrome- teorological time series and landscape attributes for
790   671 catch- ments in Great Britain, Earth Syst. Sci. Data, 12, 2459–2483, https://doi.org/10.5194/essd-12-2459-2020, 2020.

Hao, Z., Jin, J., Xia, R., Tian, S., Yang, W., Liu, Q., Zhu, M., Ma, T., Jing, C., and Zhang, Y.: CCAM: China Catchment Attributes and Meteorology dataset, Earth Syst. Sci. Data, 13, 5591–5616, https://doi.org/10.5194/essd-13-5591-2021, 2021.

795   Klingler, C., Schulz, K., and Herrnegger, M.: LamaH-CE: LArge- SaMple DAta for Hydrology and Environmental Sciences for Central Europe, Earth Syst. Sci. Data, 13, 4529–4565, https://doi.org/10.5194/essd-13-4529-2021, 2021.

Yamazaki, D., Ikeshima, D., Sosa, J., Bates, P. D., Allen, G. H., and Pavelsky, T. M.: MERIT Hydro: A high-resolution global hydrography map based on latest topography dataset, Water Resour. Res., 55, 5053-5073, https://doi.org/10.1029/2019WR024873, 2019.

800   Statistic Bulletin on China Water Activities, available at: http://www.mwr.gov.cn/english/publs/202001/t20200102_1384908.html, (last access: 12 October 2022), 2018.

Wang, J., Walter, B. A., Yao, F., Song, C., Ding, M., Maroof, A. S., Zhu, J., Fan, C., McAlister, J. M., Sikder, S., Sheng, Y., Allen, G. H., Crétaux, J.-F., and Wada, Y.: GeoDAR: georeferenced global dams and reservoirs dataset for bridging
805   attributes and geolocations, Earth Syst. Sci. Data, 14, 1869–1899, https://doi.org/10.5194/essd-14-1869-2022, 2022.

Pavlis, N. K., Holmes, S. A., Kenyon, S. C., and Factor, J. K.: The development and evaluation of the Earth Gravitational Model 2008 (EGM2008), J. Geophys. Res.-Sol. Ea., 117, B04406, https://doi.org/10.1029/2011JB008916, 2012.

Jiang, L., Andersen, O. B., Nielsen, K., Zhang, G., and Bauer-Gottwein, P.: Influence of local geoid variation on water
810   surface elevation estimates derived from multi-mission altimetry for Lake Namco, Remote Sens. Environ., 221, 65–79, https://doi.org/10.1016/j.rse.2018.11.004, 2019.

Nielsen, K., Stenseng, L., Andersen, O. B., Villadsen, H., and Knudsen, P.: Validation of CryoSat-2 SAR mode based lake levels, Remote Sens. Environ., 171, 162–170, https://doi.org/10.1016/j.rse.2015.10.023, 2015.

NASA JPL: NASA Shuttle Radar Topography Mis- sion Water Body Data Shapefiles & Raster Files, NASA EOSDIS Land
815   Processes DAAC [data set], https://doi.org/10.5067/MEaSUREs/SRTM/SRTMSWBD.003, 2013.

Papa, F., Prigent, C., Aires, F., Jimenez, C., Rossow, W. B., and Matthews, E.: Interannual variability of surface water extent at the global scale, 1993–2004, J. Geophys. Res.-Atmos., 115, D12111, https://doi.org/10.1029/2009JD012674, 2010.

Wilson, A. M., and Jetz, W.: Remotely sensed high-resolution global cloud dynamics for predicting ecosystem and biodiversity distributions, PLoS biology, 14(3), e1002415, https://doi.org/10.1371/journal.pbio.1002415, 2016.

Donchyts, G., Baart, F., Winsemius, H., Gorelick, N., Kwadijk, J., and van de Giesen, N.: Earth's surface water change over the past 30 years, Nature Clim. Change., 6, 810–813, https://doi.org/10.1038/nclimate3111, 2016.

Markert, K. N., Markert, A. M., Mayer, T., Nauman, C., Haag, A., Poortinga, A., Bhandari, B., Thwal, N. S., Kunlamai, T., Chishtie, F., Kwant, M., Phongsapan, K., Clinton, N., Towashiraporn, P., and Saah, D.: Comparing sentinel-1 surface water mapping algorithms and radiometric terrain correction processing in southeast asia utilizing google earth engine, Remote Sens., 12(15), 2469, https://doi.org/10.3390/rs12152469, 2020.

Abatzoglou, J. T., Dobrowski, S. Z., Parks, S. A., and Hegewisch, K. C.: TerraClimate, a high-resolution global dataset of monthly climate and climatic water balance from 1958–2015, Sci. Data, 5, 170191, https://doi.org/10.1038/sdata.2017.191, 2018.

Xie, J., Liu, X., Bai, P., and Liu, C.: Rapid watershed delineation using an automatic outlet relocation algorithm, Water Resour. Res., 58, e2021WR031129, https://doi.org/10.1029/2021WR031129, 2022.

Yamazaki D, Ikeshima D, Tawatari R, Yamaguchi, T., O'Loughlin, F., Neal, J. C., Sampson, C. C., Kanae, S., and Bates, P. D.: A high-accuracy map of global terrain elevations, Geophys. Res. Lett., 44, 5844-5853, https://doi.org/10.1002/2017GL072874, 2017.

Horn, B. K. P.: Hill shading and the reflectance map, P. IEEE., 69, 14–47, https://doi.org/10.1109/PROC.1981.11918, 1981.

Subramanya, K.: Engineering Hydrology, 4e, McGraw Hill Edu- cation Private Limited P-24, Green Park Extension, New Delhi, India, 2013.

Zomer, R. J., Xu, J. and Trabucco, A.: Version 3 of the Global Aridity Index and Potential Evapotranspiration Database, Sci. Data, 9, 409, https://doi.org/10.1038/s41597-022-01493-1, 2022.

Gu, L., Chen, J., Yin, J., Slater, L. J., Wang, H. M., Guo, Q., Feng, M., Qin, H., and Zhao, T.: Global Increases in Compound Flood-Hot Extreme Hazards Under Climate Warming, Geophys. Res. Lett., 49, e2022GL097726, https://doi.org/10.1029/2022GL097726, 2022.

Myneni, R., Knyazikhin, Y., and Park, T.: MCD15A3H MODIS/Terra+Aqua Leaf Area Index/FPAR 4-day L4 Global 500m SIN Grid V006 [data set], NASA EOSDIS Land Processes DAAC, https://doi.org/10.5067/MODIS/MCD15A3H.006, 2015.

Didan, K.: MODIS/Terra Vegetation Indices 16-Day L3 Global 250m SIN Grid V061 [Data set], NASA EOSDIS Land Processes DAAC, https://doi.org/10.5067/MODIS/MOD13Q1.061, 2021.

850   Running, S., Mu, Q., and Zhao, M.: MODIS/Terra Gross Primary Productivity 8-Day L4 Global 500m SIN Grid V061 [Data set], NASA EOSDIS Land Processes DAAC, https://doi.org/10.5067/MODIS/MOD17A2H.061, 2021a.

Running, S., and Zhao, M.: MODIS/Terra Net Primary Production Gap-Filled Yearly L4 Global 500m SIN Grid V061 [Data set]. NASA EOSDIS Land Processes DAAC, https://doi.org/10.5067/MODIS/MOD17A3HGF.061, 2021b.

Zeng, X.: Global vegetation root distribution for land modeling, J. Hydrometeorol., 2, 525–530, 2001.

855   Zanaga, D., Van De Kerchove, R., De Keersmaecker, W., Souverijns, N., Brockmann, C., Quast, R., Wevers, J., Grosu, A., Paccini, A., Vergnaud, S., Cartus, O., Santoro, M., Fritz, S., Georgieva, I., Lesiv, M., Carter, S., Herold, M., Li, Linlin, Tsendbazar, N. E., Ramoino, F., and Arino, O.: ESA WorldCover 10 m 2020 v100, https://doi.org/10.5281/zenodo.5571936, 2021.

Hengl, T., Mendes de Jesus, J., Heuvelink, G. B., Ruiperez Gonzalez, M., Kilibarda, M., Blagotic´, A., Shangguan, W., Wright, M. N., Geng, X., and Bauer-Marschallinger, B.: SoilGrids250m: Global gridded soil information based on machine learning, PLoS one, 12, e0169748, https://doi.org/10.1371/journal.pone.0169748, 2017.

860

Shangguan, W., Dai, Y., Liu, B., Zhu, A., Duan, Q., Wu, L., Ji, D., Ye, A., Yuan, H., and Zhang, Q.: A China data set of soil properties for land surface modeling, J. Adv. Model. Earth Sy., 5, 212–224, https://doi.org/10.1002/jame.20026, 2013.

865   Dai, Y., Xin, Q., Wei, N., Zhang, Y., Shangguan, W., Yuan, H., Zhang, S., Liu, S., and Lu, X.: A global high-resolution data set of soil hydraulic and thermal properties for land surface modeling, J. Adv. Model. Earth Sy., 11, 2996–3023, https://doi.org/10.1029/2019MS001784, 2019.

Shangguan, W., Dai, Y., Duan, Q., Liu, B., and Yuan, H.: A global soil data set for earth system modeling, J. Adv. Model. Earth Sy., 6, 249–263, https://doi.org/10.1002/2013MS000293, 2014.

870   Hartmann, J. and Moosdorf, N.: The new global lithological map database GLiM: A representation of rock properties at the Earth surface, Geochem. Geophy. Geosy., 13, 1–37, https://doi.org/10.1029/2012GC004370, 2012.

Gleeson, T., Moosdorf, N., Hartmann, J., and van Beek, L. P. H.: A glimpse beneath earth's surface: GLobal HYdrogeology MaPS (GLHYMPS) of permeability and porosity, Geophys. Res. Lett., 41, 3891–3898, https://doi.org/10.1002/2014GL059856, 2014.

875   Gleeson, T.: GLobal HYdrogeology MaPS (GLHYMPS) of per- meability and porosity, Scholars Portal Dataverse, V1 [data set], https://doi.org/10.5683/SP2/DLGXYO, 2018.

Huscroft, J., Gleeson, T., Hartmann, J., and Börker, J.: Com- piling and Mapping Global Permeability of the Unconsolidated and Consolidated Earth: GLobal HYdrogeology MaPS 2.0 (GLHYMPS 2.0), Geophys. Res. Lett., 45, 1897–1904, https://doi.org/10.1002/2017GL075860, 2018.

880   Center for International Earth Science Information Network – Columbia University: Gridded Population of the World,
       Version 4 (GPWv4): Population Count, Revision 11, NASA [data set], https://doi.org/10.7927/H4JW8BX5,
       2018.

       Venter, O., Sanderson, E. W., Magrach, A., Allan, J. R., Beher, J., Jones, K. R., Possingham, H. P., Laurance, W. F., Wood, P.,
       Fekete, B. M., Levy, M. A., and Watson, J. E. M.: Global ter- restrial Human Footprint maps for 1993 and 2009,
885   Sci. Data, 3, 160067, https://doi.org/10.1038/sdata.2016.67, 2016.

       Doll, C. N.: CIESIN Thematic Guide to Night-Time Light Remote Sensing and Its Applications, Center for International
       Earth Science Information Network, Palisades, NY, USA, 41 pp., 2008.

       Meijer, J., Huijbregts, M., Schotten, K., and Schipper, A.: Global patterns of current and future road infrastructure,
       Environ. Res. Lett., 13, 064006, https://doi.org/10.1088/1748-9326/aabd42, 2018.

890   Tiwari, A.D., and Mishra, V.: Prediction of reservoir storage anomalies in India, J. Geophy. Res. Atmos., 124, 3822–3838,
       doi: 10.1029/2019JD030525, 2019.

       Di Baldassarre, G., Wanders, N., AghaKouchak, A., Kuil, L., Rangecroft, S., Veldkamp, T. I. E., Garcia, M., van Oel, P. R.,
       Breinl, K., and Van Loon, A. F.: Water shortages worsened by reservoir effects. Nat. Sustain., 1, 617–622,
       https://doi.org/10.1038/s41893-018-0159-0, 2018.

895   Faucheux, N. M., Sample, A. R., Aldridge, C. A., Norris, D. M., Owens, C., Starnes, V. R., VanderBloemen, S., and Miranda, L.
       E.: Reservoir attributes display cascading spatial patterns along river basins. Water Resources Research, 58,
       e2021WR029910, https://doi.org/10.1029/2021WR029910, 2022.

       Null, S. E., Medellín-Azura, J., Escriva-Bou, A., Lent, M., and Lund, J. R.: Optimizing the dammed: Water supply losses and
       fish habitat gains from dam removal in California. J. Environ. Manage., 136, 121–131,
900   https://doi.org/10.1016/j.jenvman.2014.01.024, 2014.